Accepted manuscript (author version)

To appear in:

Iranian Journal of Earth Sciences (Iran J. Earth. Sci.)

E-ISSN: 2228-785X Print ISSN: 2008-8779

Received: 13 November 2024

Revised: 25 March 2025

Accepted: 23 August 2025

DOI: https://doi.org/10.57647/j.ijes.2025.17565

Original Research

Fusion of K-Means, Fuzzy C-Means, SAM, and SVM for hydrothermal alteration mapping using ASTER data: A case study from the Zafarghand porphyry copper region, Central Iran

Seyyed Saeed Ghannadpour[1*], Samane Esmaelzade Kalkhoran[1], Amin Beiranvand Pour[2]

[1] Department of Mining Engineering, Amirkabir University of Technology (Tehran Polytechnic), Tehran, Iran

[2] Institute of Oceanography and Environment (INOS), Higher Institution Center of Excellence (HICoE) in Marine Science, University Malaysia Terengganu (UMT), Kuala Nerus 21030, Terengganu, Malaysia

* Corresponding author: s.ghannadpour@aut.ac.ir

Abstract

Machine learning (ML) algorithms can be applied to remote sensing satellite imagery to improve the accuracy of mineral and lithology mapping in the initial stages of a mineral exploration program. In this study, both unsupervised and supervised ML algorithms, namely K-Means clustering, Support Vector Machine (SVM), Fuzzy C-Means (FCM) clustering, and Spectral Angle Mapper (SAM), are evaluated and fused for the accurate mapping of alteration zones in the Zafarghand porphyry Cu region in central Ir an using ASTER satellite imagery. The alteration zones of potassic, phyllic, argillic, propylitic, and silicification were documented in the Zafarghand porphyry deposit, which could be identified and mapped with ASTER satellite images and ML algorithms. The ML algorithms analysed the digital pixel numbers (DNs) of the satellite images from the ASTER sensor to determine hydrothermal alteration zones. K-Means clustering was used for grouping the data, while SVM was used for categorization and prediction. K-Means clustering achieved an accuracy of 78.83%, while the SVM method achieved an accuracy of 98.25% in identifying hydrothermal alteration zones, especially propylitic and phyllic alteration zones. Moreover, stacking the bands and applying FCM clustering with SAM improved the precision of hydrothermal alteration detection, and the accuracy of K-Means-SVM after stacking reached 96.2%. Using the fusion of these ML algorithms, a thorough investigation of alteration zones was developed, improving the overall accuracy and effectiveness of the alteration mapping procedure. The developed ML-based approach was then used to create a map of hydrothermal alteration in the Zafarghand porphyry Cu region, which was verified in field investigations and petrographic analyses. The Xie-Beni index for FCM clustering was 0.25833, indicating high accuracy and reliability in the clustering process. The results show that the fusion of supervised and unsupervised ML algorithms, such as K-Means-SVM, combined with methods like FCM clustering and SAM, has the potential to identify complex geological features and significantly improve the porphyry Cu exploration program at low cost.

Keywords: Machine Learning algorithms, ASTER, Advanced image processing, Fusion, K-Means-SVM, FCM clustering, SAM, Hydrothermal alteration zones, Alteration mapping, Porphyry Cu exploration, Iran.

1. Introduction

Remote sensing is a effective prospecting technique in the field of spectral detection of minerals, which plays an important role in identifying specific types of hydrothermal alteration in different regions. In addition, this technique is employed in the study of surface geochemical reactions (such as the oxidation of sulfide minerals) and also in the study of volcanic phenomena (Bishop and Murad, 2005; Yousefi et al., 2018). Most hydrothermal deposits have been identified and investigated due to the distinctive spectral signatures of altered minerals inside the SWIR spectral region (range 2 to 2.5 micrometers) (Yousefi et al 2018).

Image processing techniques are chiefly utilized to improve satellite imagery, carry out feature extraction and recognition, execute classification, and monitor change detection (Asokan et al., 2020). Such procedures employ assorted mathematical algorithms to derive meaningful information (Babbar and Rathee, 2019). Of these approaches, ML techniques, within the realm of machine intelligence, are considered reliable as they are able to classify remote sensing images accurately and efficiently. ML facilitates handling of multidimensional datasets and the allocation of attributes possessing intricate properties (Maxwell et al., 2018). The integration of remote sensing data and advanced techniques such as ML algorithms supports and optimizes the mineral prospecting process by performing spectral classifications; therefore, ML methods have gained more attention as an approach to issues in geology and resource prospecting. As a robust empirical framework, ML is capable of performing regression and classification, under both supervised and unsupervised modes, for nonlinear system modeling. These systems could comprise a few variables or thousands of variables. In ML, training data are comprehensively prepared so that the parameter domain of the system is covered as fully as attainable. Often, a random share of these data is set aside for independent validation. ML methods are well suited to challenges where theoretical comprehension is lacking, while a significant quantity of observational evidence and data exists for utilization. Ideally, if the theoretical knowledge is complete, the use of ML would be unnecessary (Mitchell, 1997; Gewali et al., 2018; Sun and Scanlon 2019; Khosaravi et al., 2020; Salkuti 2020; Moghadam et al., 2021). To verify the proper functioning of this algorithm, new data inputs are supplied to the ML model and its predictions are then evaluated. If the produced outcomes fail to match expectations, the model is subjected to repeated retraining until the required or intended result is eventually obtained. This design allows the ML algorithm to continue learning independently using the data and to supply the best answers possible, with accuracy gradually improving as more iterations are performed (Carranza and Laborte, 2016; Zuo and Carranza, 2023).

Modern image processing and remote sensing applications require the use of supervised and unsupervised ML algorithms. Supervised algorithms, such as Support Vector Machines (SVMs), are beneficial for high accuracy tasks, such as object detection and image classification, as they learn decision boundaries from labeled training data (Lu et al 2023). As often mentioned in the literature, SVM are particularly favored because they can handle high-dimensional data and perform effectively even with a small number of training examples. Unsupervised algorithms, such as K-Means clustering, on the other hand, work without labeled data and are mainly used for data segmentation or grouping by innate patterns. K-Means clustering is popular for its ease of use, scalability, and effectiveness when working with large data sets, making it perfect for pre-processing steps where clusters need to be found in image data. The complementary qualities of SVM and K-Means clustering are the reason for their prominent position in advanced image processing: while K-Means clustering is well suited for exploratory data analysis, feature extraction, and preliminary segmentation, SVM provide accurate classification. This combination of supervised and unsupervised techniques is well known (Bekaddour et al., 2015).

Classification maps are the most important result of image processing in remote sensing. In recent years, data-driven approaches have become increasingly important in remote sensing. Especially non-parametric methods have proven to be very powerful. This overview covers both supervised and unsupervised methods. In supervised image classification, information about the class membership of individual pixels, which are labeled by experts, is used to create a model that can be generalized to the entire image or a set of images. Currently, the most successful methods are neural networks and SVM (Huang et al., 2002; Foody and Mathur, 2004; Benediktsson et al., 2005; Camps-Valls and Bruzzone, 2005; Del Frate et al., 2007). Algorithms create functions that map inputs to desired outputs. In supervised learning, a typical task is classification, where the learner must approximate a function that maps a vector to one of several classes by examining numerous input-output examples of the function (Tou and Gonzalez 1974; Osisanwo et al., 2017; Abdullah and Abdulazeez, 2021; Shuo and Ming, 2022). Unsupervised classification of remote sensing images has many applications, e.g., visualization and monitoring of similar areas within a scene or as a preprocessing step for supervised classifiers. Numerous clustering methods have been developed to address this problem. These methods identify patterns in unlabeled data (Bezdek, 2013; Mahesh, 2020; Naeem et al., 2023).

VNIR and SWIR spectral bands have the appropriate resolution to identify and define specific spectral patterns of carbonate minerals, hydrate- and hydroxyl-bearing sulfate, silicates and other minerals that have significant absorption characteristics in the SWIR region (Khaleghi et al., 2020). The SWIR bands cover the Al-O-H, Si-O-H, and Mg-O-H absorption ranges, making them effective for their identification (Gupta, 2003; Li et al., 2014; Ramsey and Flynn, 2020).

There are still significant challenges and crucial gaps in the application of ML techniques for comprehensive classification and advanced processing of remote sensing imagery (e.g., ASTER) for mineral exploration. The fusion of ML techniques is very promising for enhanced hydrothermal alteration mapping of porphyry Cu systems, especially using the SWIR bands of ASTER data. The fusion of K-Means clustering, FCM clustering, and Spectral Angle Mapper (SAM) with SVM can improve the overall precision and effectiveness of the alteration zones of porphyry Cu systems by leveraging both clustering and spectral analysis techniques. While SAM improves spectral discrimination, especially for hydrothermal minerals, FCM clustering offers a more flexible partitioning of alteration zones. By taking advantage of both methods, this two-step approach increases the ability of satellite image processing to identify complex geologic features. Combining directed learning with self-regulation techniques can significantly improve hydrothermal alteration mapping methods and potentially be cost and time effective. Mineral exploration programs can be advanced with fused ML techniques when used in conjunction with human supervision and without direct control (Yousefi et al., 2021, Lachaud et al., 2023).

In this research, ASTER satellite images and implementation of K-Means and FCM clustering, SAM, and SVMs on enhanced hydrothermal alteration in central Iran's Zafarghand porphyry Cu region were evaluated. Despite the advancements in remote sensing, accurately identifying alteration zones in complex geological settings remains challenging. These difficulties primarily stem from spectral overlaps, lithological diversity, and inconsistencies in surface cover, necessitating more advanced techniques that are highly sensitive to subtle anomalies. Cu and Mo are critical elements in modern technologies and the production of clean energy. Porphyry Cu-Mo systems represent the primary sources of these elements and typically consist of extensive rock volumes altered by hydrothermal processes associated with porphyritic intrusions. In recent years, the advent of advanced satellite remote sensing technologies has emerged as an effective tool for mapping alteration zones related to these systems, thereby supporting copper exploration efforts (Fu et al., 2023; Fallaha et al., 2024; Rahmani et al., 2025; Jain et al., 2025). The Zafarghand porphyry Cu region is located within the Urmia-Dokhtar magmatic arc (UDMA) (Fig. 1a). Previous studies in this region have included geologic mapping, geophysical surveys, geochemical studies, stable isotope and chemistry studies, and mineralogical and geochemical analyses of hydrothermal alteration zones (Sadeghian and Ghaffary, 2011; Aminoroayaei Yamini et al., 2016; Aminoroayaei Yamini et al., 2017; Mohammadi et al., 2018; Ghannadpour et al., 2024b). Several studies have already been conducted on the geological aspects of the Zafarghand porphyry Cu region. However, there is a paucity of remote sensing analysis to map the alteration zones using ML algorithms accurately. This investigation intends to overcome the gap by exploring alteration zones in the study area via ASTER data and implementing advanced ML–based image analysis techniques. Hydrothermal alteration zones spectral properties have also been enhanced by stacking ASTER bands before using ML algorithms, which has resulted in a more accurate classification. Consequently, the following main objectives were set: (1) to evaluate the K-Means clustering and SVM for mapping hydrothermal alteration zones using ASTER's SWIR bands; (2) to fuse K-Means clustering results and SVM to produce an accurate map of hydrothermal alteration zones in the Zafarghand porphyry Cu region; (3) to developed a ML-based approach for advanced image processing of remote sensing imagery to identify hydrothermal alteration zones associated with porphyry Cu deposits. (4) to enhance classification precision and hydrothermal mineral differentiation by integrating FCM clustering and SAM into the alteration mapping process.

2. Geological setting of the study area

Many of the known porphyry Cu deposits such as Sarcheshmeh, Miduk, Dalli, Kahang, Zafarghand and Zefreh in Iran are located in the UDMA, also known as the Central Iranian

Volcanic-Plutonic Belt (Varmazyari et al., 2025). The intrusive rocks and copper deposits in this arc were formed when the Neo-Tethys was abducted beneath the central part of Iran in the middle Miocene. The rocks in this area are mainly diorite, granodiorite and granitoid, while the volcanic rocks are andesite, dacite and pyroclastics (Alaminia et al., 2017). The Zafarghand porphyry Cu deposit is located in the Urumieh-Dohktar Magmatic Arc. It lies in the western part of Zafarghand (geologic sheet 1:100,000 Ardestan), which extends from 55°23'52"E to 30°26'52"E longitude and 52°11'33"N to 30°10'33"N latitude (Fig.1b) (Alaminia et al., 2017). The Zafarghand copper exploration zone is located around 110 kilometers northeast of Isfahan in southeast Ardestan, central Iran.

Field investigations and petrographic analyses carried out in the area have identified a series of acidic to intermediate igneous rocks, comprising both volcanic and intrusive formations, from the Upper Eocene onwards. These rock units are delineated as follows (Alaminia et al., 2017). Rhyolite, characterized by limited outcrops in the northwest corner, exhibits a pinkish-gray hue (Fig.1c). These rocks typically exhibit a porphyritic texture with a glassy flow. Dacites and rhyodacites, which extend over much of the area, exhibit gray to greenish hues (Fig.1c). This unit is considered the most important host rock for copper mineralization in the region. It is characterized by a porphyritic texture with a fine-grained, amorphous, and porous felsic matrix. The andesites, which predominate in the southwestern and western regions, appear dark gray and are characterized by their hollow nature due to the abundance of coarse crystals. Intrusive formations, including diorite, quartz diorite, and microdiorite, are observed in the northwestern and southeastern parts and are dark gray in color (Fig.1c). A semi-intrusive porphyritic quartz and diorite mass occupies a smaller area in the southeastern section of the region (Fig.1c) (Alaminia et al., 2017).

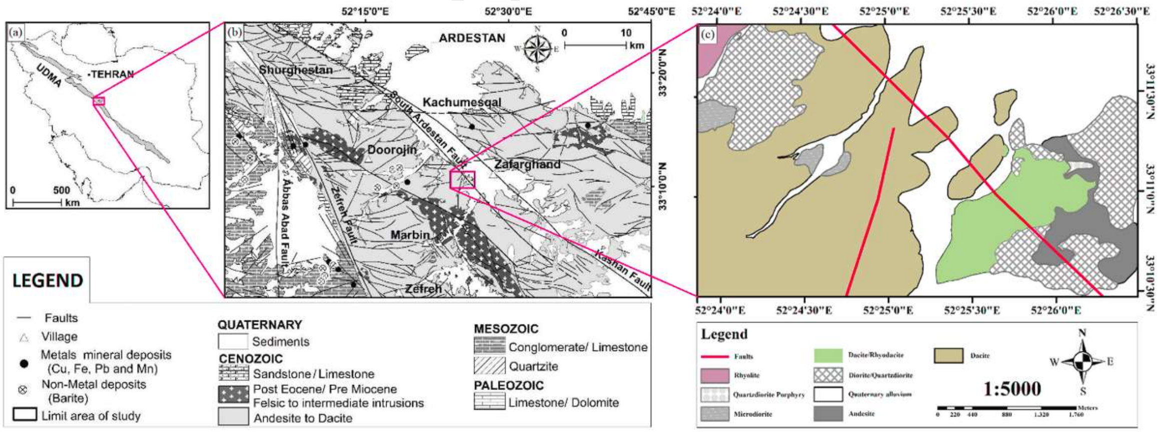

Figure 1. (a) The Zafarghand exploration area situated in the central UDMA; (b) simplified geological map segment of Ardestan and Shahrab with scale 1:100,000; (c) simplified geological map of the Zafarghand region, redrawn and modified from Alaminia et al., 2017

Studies previously carried out in the region identified several hydrothermal alteration zones, namely potassic, phyllic, siliceous, argillic, and propylitic (Esmailzadeh Kalkhoran et al., 2024). Hydrothermal alterations commonly appear close to intrusive masses and surrounding rocks along the South Ardestan Fault (Fig.2). Potassic alteration in the southeast is mostly restricted to the vicinity of quartz diorite, whereas phyllic alteration is noted around intrusive diorite, porphyritic quartz diorite, and also in dacite–rhyodacite volcanics. To a lesser extent, phyllic alteration is replaced by siliceous and argillic types (Fig.2) (Ghannadpour et al., 2024). On the other hand, propylitic alteration is extensively developed in the deposit's outer zone. The wide occurrence of chlorite in southern Ardestan highlights that alteration phenomena are widespread throughout the region (Fig.2). Alteration of phyllic rocks in this area is characterized by the presence of extensive quartz-sericite, stockwork of quartz veins, and iron oxide (mainly hematite) in porphyritic dacites and quartz diorites. Some iron oxide and quartz veins up to 2 centimeters thick are visible in this alteration (Alaminia et al., 2017; Ghannadpour et al., 2024).

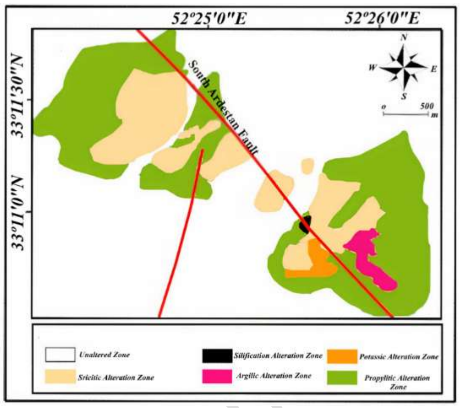

Figure 2. Alteration zones in Zafarghand region (based on modifications from (Alaminia et al., 2017))

3- Spectral properties of alteration minerals

Porphyry Cu deposits are usually controlled by hydrothermal alteration zones (Lowell and Gilbert 1970) that have a regional or tens-of-meter scale of quartz and potassium-rich core with several incremental zones of alteration surrounding it. The sixth ASTER band is positioned near the principal Al–OH absorption feature of the phyllic alteration zone, dominated by illite/muscovite (sericite) at 2.20 µm. The argillic zone, narrower in distribution and located next to it, contains both kaolinite and alunite, which together create a secondary Al–OH absorption at 2.17 µm corresponding to ASTER band 5. It moves outwards, and the propylitic zone is formed in its periphery, defined by a mineral assemblage of epidote, chlorite, and calcite. The minerals show well-resolved absorption of 2.35 µm, well-matched with ASTER band 8. It is this spectral alteration signature that underlies the creation and mapping of potential target areas in porphyry systems (Fig.3) (Clark et al., 1990; Dalton et al., 2004; Rowan et al., 2006; Pour and Hashim, 2012).

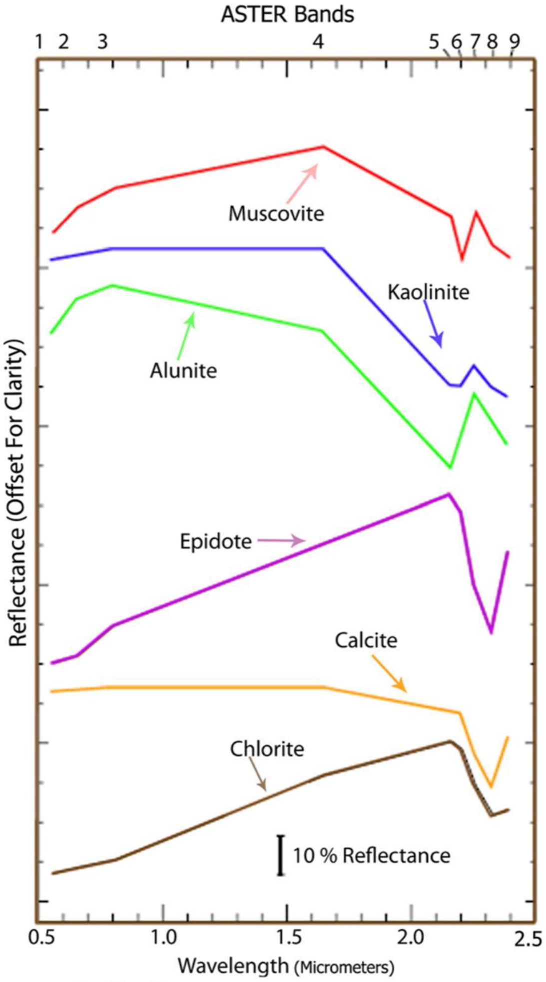

Figure 3. For muscovite, kaolinite, alunite, epidote, calcite, and chlorite, laboratory-based NIR spectra were resampled into ASTER band intervals. Characteristic absorption bands occur at 2.20 µm for muscovite (phyllic), 2.17 µm for kaolinite–alunite (argillic), and 2.35 µm for epidote, calcite, and chlorite (propylitic) (Clark et al., 1993; adapted from Mars & Rowan, 2006)

Materials and methods

4.1.ASTER data and pre-processing

The ASTER sensor, offers adequate spectral detail in SWIR bands and thus proves effective for mapping hydrothermal alteration related to porphyry Cu systems and epithermal Au deposits (Pour and Hashim, 2011; Moradpour et al., 2022). In total, ASTER imagery contains 14 bands: three are collected in the VNIR domain at 15 m resolution, six fall within the SWIR domain at 30 m, and five belong to the TIR domain, each with a 90 m spatial resolution. An area of 60 by 60 kilometers is covered by each image scene. This sensor is capable of detecting alteration associated with minerals such as kaolinite, sericite and chlorite, which are important indicators of porphyry Cu mineralization. Given the spectral capabilities and high resolution of ASTER, this sensor can accurately identify mineralogical compositions associated with alteration and can be used as a valuable tool in mineral exploration (Kumar et al., 2015). This study utilized an ASTER L1T scene (AST_L1T_00308182002072145_20150424120125_9911) that was acquired on July 21, 2002 (see Fig.4). Pre-processing of ASTER imagery involves radiometric calibration, atmospheric adjustment, as well as geometric orthorectification procedures. The IARR method calculates the average reflectance of the entire image and normalizes each pixel's reflectance by dividing its Digital Number (DN) value by the mean DN value of the corresponding band. This process helps in analyzing relative reflectance variations across the image. The essential premise is that the mean spectrum reflects the spectrum of the sun (Ghannadpour et al., 2024; Esmailzadeh Kalkhoran et al., 2024; Esmaelzadeh Kalkhoran et al., 2024; Ghannadpour et al., 2024b). In addition to radiometric and atmospheric corrections, image normalization using the IARR method helps mitigate variations caused by changes in brightness and sensor viewing angles. This normalization results in more uniform light intensity across the image, enabling more accurate comparisons of pixel values and improving the reliability of analyses such as classification and spectral interpretation. By reducing noise and standardizing reflectance values, algorithms can more effectively detect subtle spectral variations associated with alteration minerals—an essential factor in geologically complex regions.

4.2. Data used and preparation

ASTER's SWIR bands (4–9) were selected in order to extract each pixel's DN values. These selected bands correspond with prior studies (Ghannadpour and Esmaelzadeh Kalkhoran, 2024a) of porphyry Cu deposits, as their absorption and reflectance behavior is particularly effective in enhancing the visibility of associated alteration zones. Fig. 4(a) shows the entire ASTER image as an RGB composite, whereas Fig.4(b) highlights a subset over the Zafarghand porphyry Cu deposit. Resolution decreases since the study area is significantly smaller than the ASTER sensor's field of view, a condition that constrains the number of pixels available (Esmaelzadeh Kalkhoran et al., 2024). Nevertheless, the individual pixels remain valuable patterns with specific coordinates. This property is beneficial for ML applications as it allows for a more targeted analysis of the data and a more precise evaluation of the effectiveness of the method. Although the overall quality of the image is compromised, the pixel-level information is still crucial for accurate modeling.

Figure 4. (a): RGB for 468 bands of ASTER whole scene (b): A subset image of the RGB for 468 bands covering the Zafarghand porphyry Cu deposit

First, the ASTER sensor images were resized using ENVI software to obtain better results and higher accuracy of the applied model. Then MATLAB software was used to apply ML algorithms. Based on studies carried out with the ASTER sensor on porphyry Cu deposits, the SWIR bands were identified as the most critical for highlighting the alterations of porphyry Cu deposits. These bands are particularly effective due to their reflectance and absorption characteristics, especially concerning the desired alteration zones (e.g., phyllic and propylitic) (Hunt, 1971; Grove et al., 1992; Salisbury and D'Aria, 1992; Mhangara, 2005; Vicente and de Souza Filho, 2011; Pour and Hashim, 2011; Pour and Hashim, 2012; Nouri et al., 2012; Shahi and Kamkar Rouhani., 2014; Sadek et al., 2015; Kumar et al., 2015; El-Qassas et al., 2023). Fig.5 shows histograms for the DNs of the SWIR bands of the ASTER image. As demonstrated in these histograms, the distribution is normal; therefore, renormalization is not required. However, if the distribution is not normal, various techniques can be applied for normalization (Ghannadpour and Hezarkhani, 2023).

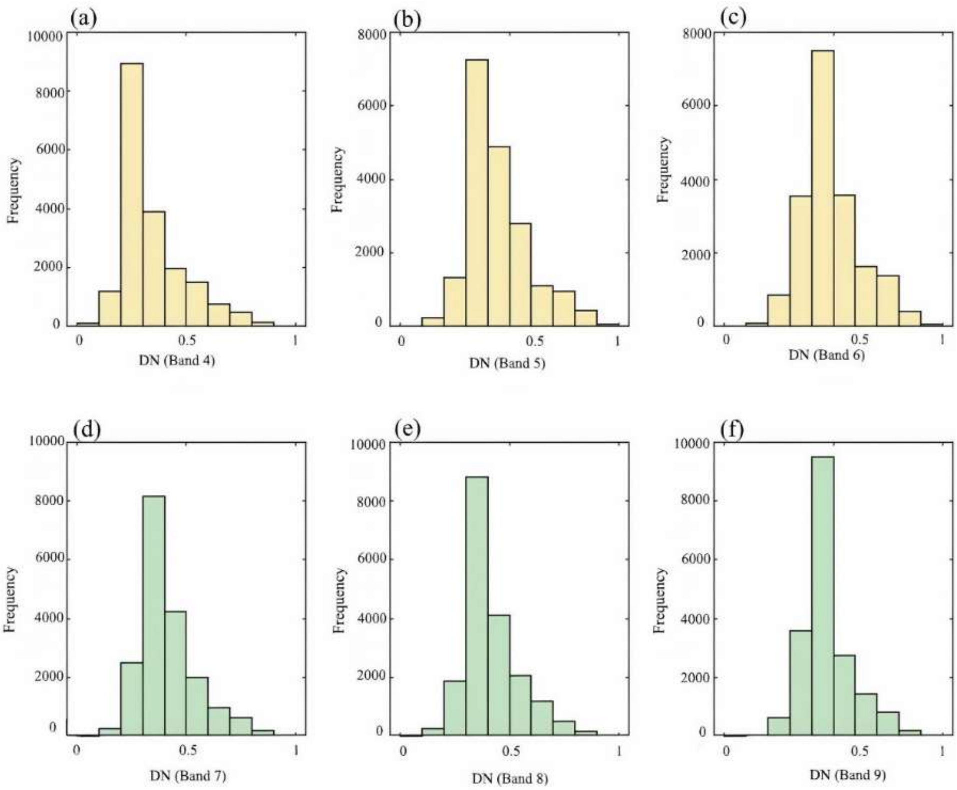

Figure 5. The frequency diagram of DN value for SWIR bands of ASTER image (a-f)

4.3. Image processing techniques

Fig. 6 displays the methodological flowchart for applying the K-Means clustering, FCM clustering, SAM, and SVM Classification algorithms to the processing of the ASTER image's SWIR bands. The workflow and individual steps are depicted in this flowchart. Initial corrections are made to eliminate errors that may have existed after the ASTER satellite images are acquired and the DNs are extracted. Next, to enhance spectral discrimination, the SWIR bands are stacked. For clustering, the FCM clustering technique is applied in conjunction with K-Means clustering, and the clusters that are produced are used as training data for the SVM model. Additionally, to improve alteration zone recognition, the SAM is included. The final hydrothermal alteration map is created by combining the categorized layers following the use of the SVM algorithm, which enhances accuracy and distinguishes geological features.

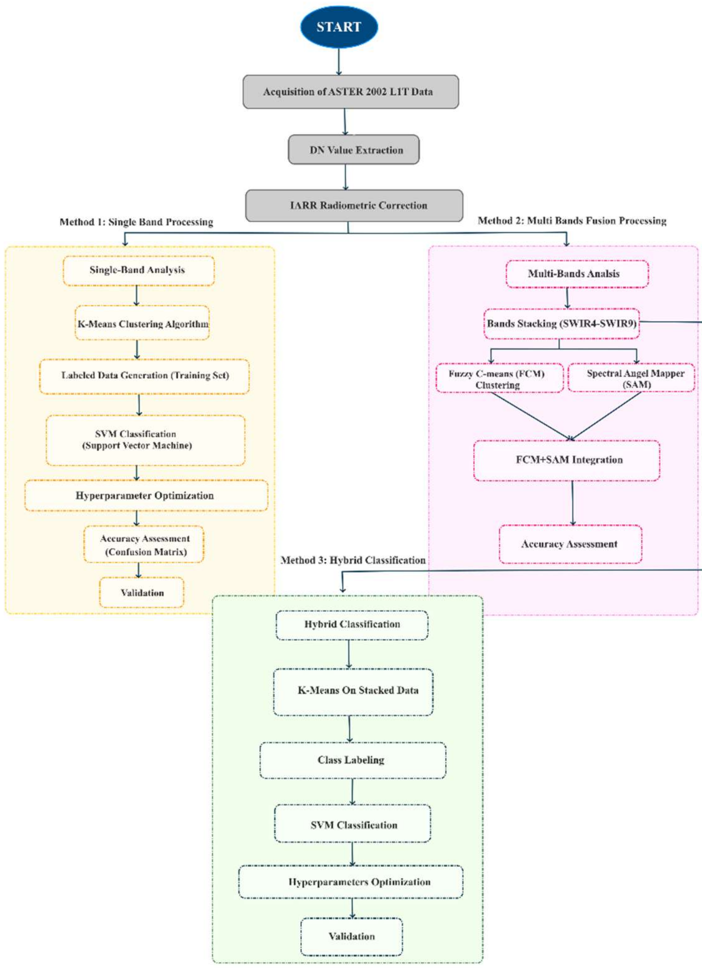

Figure 6. An overview of methodological flowchart for processing the ASTER data using ML algorithms

4.3.1 K-Means clustering algorithm

Feature extraction is a crucial step in any recognition system. Its purpose is to identify the most important features of the image and use this concise information to classify the entire image. The choice of features has a significant impact on the classification process; good features lead to a higher recognition success rate, while poor features lead to lower accuracy (Arai and Barakbah, 2007). In K-Means clustering, the first step is defining K, the cluster number, followed by selecting K centroids. Objects are then stochastically allocated to the closest centroid under the nearest-neighbor rule, thereby forming clusters (Maulik and Bandyopadhyay, 2000), then calculating the mean value of each cluster and setting this value as the new clustering centroid (Abdalameer et al., 2022). The procedure is repeatedly iterative and is governed by the error function E The error function is as follows [Eq. (2)]:

$$E = \sum_{i=1}^{k} \sum_{p \in C_i} (p - m_i) \tag{2}$$

In this context, p designates the spatial object, while mi indicates the centroid of cluster C_i. A lower E shows higher similarity of the grouped data. In this method, spectral data is collected from satellite images or other sources and pre-processed. After applying the atmospheric correction to the DNs of the SWIR bands of ASTER image, the number of classes for this method was set to 3 classes according to previous studies and alteration map of the study area (see Fig.2).

4.3.3. Fuzzy C-Means (FCM) clustering

The main feature of FCM clustering is that a vector can belong to multiple clusters simultaneously. In contrast, traditional clustering methods assign each vector exclusively to a specific cluster (Li and Shen, 2010). The process and steps of FCM clustering are shown in Fig.7.

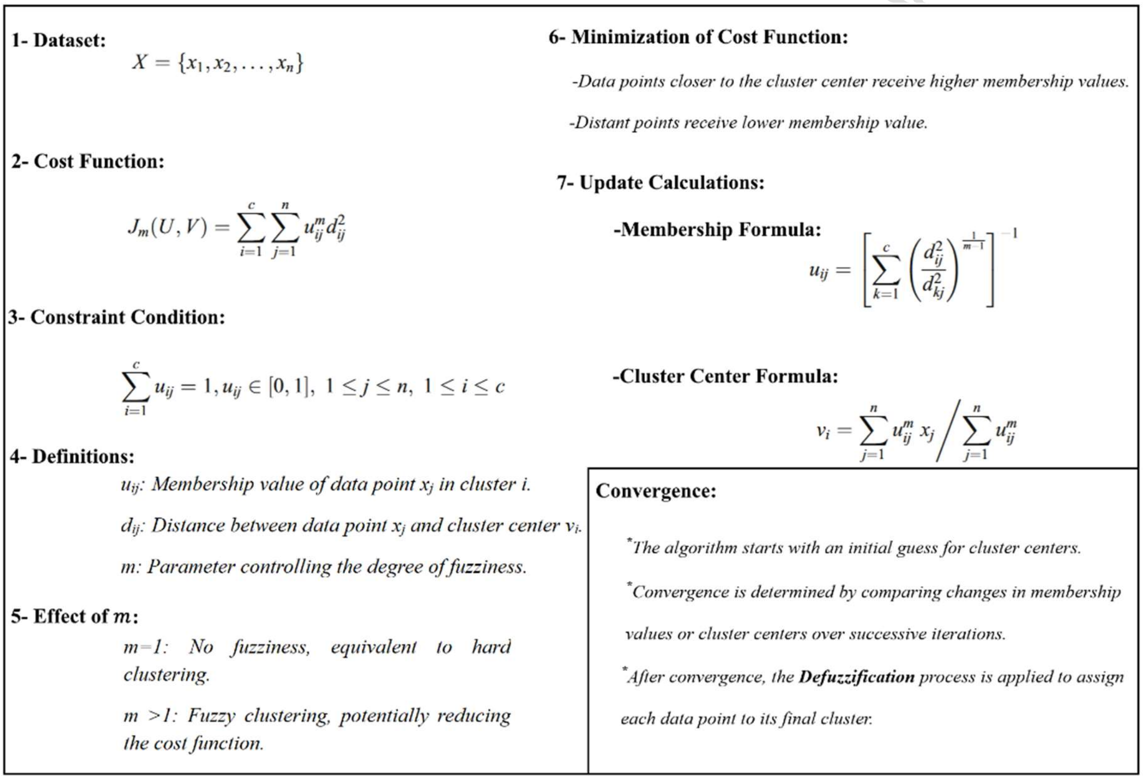

Figure 7. Steps and process of FCM clustering

4.3.4. Spectral Angle Mapper (SAM)

The SAM method is extensively employed for lithological mapping and has been adopted in many investigations (Chen et al., 2007; Murphy et al., 2012). This algorithm, which operates based on spectral angle calculations, is a supervised classification method for remote sensing imagery. Spectral signatures of the image, in this technique, are represented as vectors located in a multidimensional feature space, the dimensions of which are defined by the count of spectral bands in the image (Kruse et al., 1993).

The SAM classification process is based on calculating the angle between the spectral signatures of the image and those of the reference spectra. Reference spectra may come from field observations or existing spectral libraries (Kruse et al., 1993). This method provides an overall assessment of spectral similarity across the entire spectral range of interest or within a specific portion of it (Hecker et al., 2008).

4.3.5. SVM classification algorithm

Parametric classification objective to specify the representative values or statistical distribution of features for each class. In comparison, SVM pays attention primarily to training samples positioned close to the separating hyperplane that best divides classes (Cortes, 1995; Huang et al., 2002; Pal, 2005; Mountrakis et al., 2011; Pal and Foody, 2012). Known as support vectors, these essential samples lend their name to the method. SVM aims to identify the best boundary that enlarges the margin between the respective support vectors. SVM classifiers are intrinsically binary; thus, to distinguish among classes, the algorithm is applied to all possible pairs. This approach can exponentially increase computational time as the total number of classes becomes larger (Cortes, 1995). Originally, SVMs were developed to determine a linear class boundary or hyperplane. This limitation is solved by projecting the feature space into a higher dimension where a linear boundary may exist. This technique, known as the kernel trick, involves different kernels, each with different user-defined parameters (Kavzoglu and Colkesen, 2009). In this study, the Radial Basis Function (RBF) kernel was employed due to its strong capability in handling nonlinear class boundaries. Given the complex spectral patterns and overlapping alteration zones—such as argillic, phyllic, and propylitic—the RBF kernel offers a more flexible decision boundary within high-dimensional feature space. Its effectiveness in remote sensing applications is also well documented in the literature (Huang et al., 2002; Kavzoglu and Colkesen, 2009). Remote sensing applications often make use of polynomial and RBF kernels (Huang et al., 2002). For classes that are not inherently separated, the decision boundary can be described as a soft boundary. This allows some training patterns to be on the wrong side of the boundary, with the user specifying a penalty through the parameter C (Cortes, 1995). Higher C values create a complicated decision boundary and lower generalization ability.

Supervised algorithms require training data. Therefore, the results of K-Means clustering and the created classes are used as input and training data for the model. Finally, the SVMs model algorithm is applied to the DN of the pixels considering the pixel coordinates.

5. Analysis and results

5.1. K-Means clustering outputs

Clustering was performed using the SWIR spectral bands obtained from the ASTER sensor. According to the alteration map and knowledge of the study area, three classes were considered suitable for this method (see Fig.2), was suitable for three classes. The results of this method are shown in Fig.5. The method effectively separated the regional variations, demonstrating the performance of the algorithm in classifying satellite images. The silhouette criterion, one of four evaluation criteria for clustering, was used to evaluate the model. This criterion measures how well each pixel belongs to its assigned cluster compared to the neighboring clusters. The silhouette index varies between –1 and 1; values approaching 1 suggest proper, high-quality clustering, whereas negative values reflect clustering that has been assigned incorrectly. This criterion allows the evaluation of the overall model, individual clusters, and individual pixels. In general, an average silhouette criterion above 0.2 indicates a suitable clustering model (Wang et al., 2017). Fig.8 (a-f) shows result of K-Means clustering applied to SWIR bands. The phyllic and propylitic alterations present in the region were clustered using the K-Means clustering algorithm. Comparing the obtained results with the regional alteration map (Fig.2) reveals that green zones correspond to phyllic alteration, whereas purple zones correspond to propylitic alteration. This observation shows that the method used worked effectively in this area.

Accuracy of results and number of classes for K-Means clustering are shown in Table 1. Evaluation of K-Means clustering performance for different bands was carried out by applying the silhouette score. The metric assesses clustering performance by analyzing the compactness of samples in each cluster and the separation among clusters. As an index of clustering performance, the silhouette score shows how strongly samples belong to their clusters—high scores denote good separation, near-zero scores mark boundary cases, and negative ones reveal misclassified instances. According to the table, clustering is performed effectively in all bands. The silhouette scores are consistently above zero and approaching 1, indicating that the samples were correctly assigned to their respective clusters.

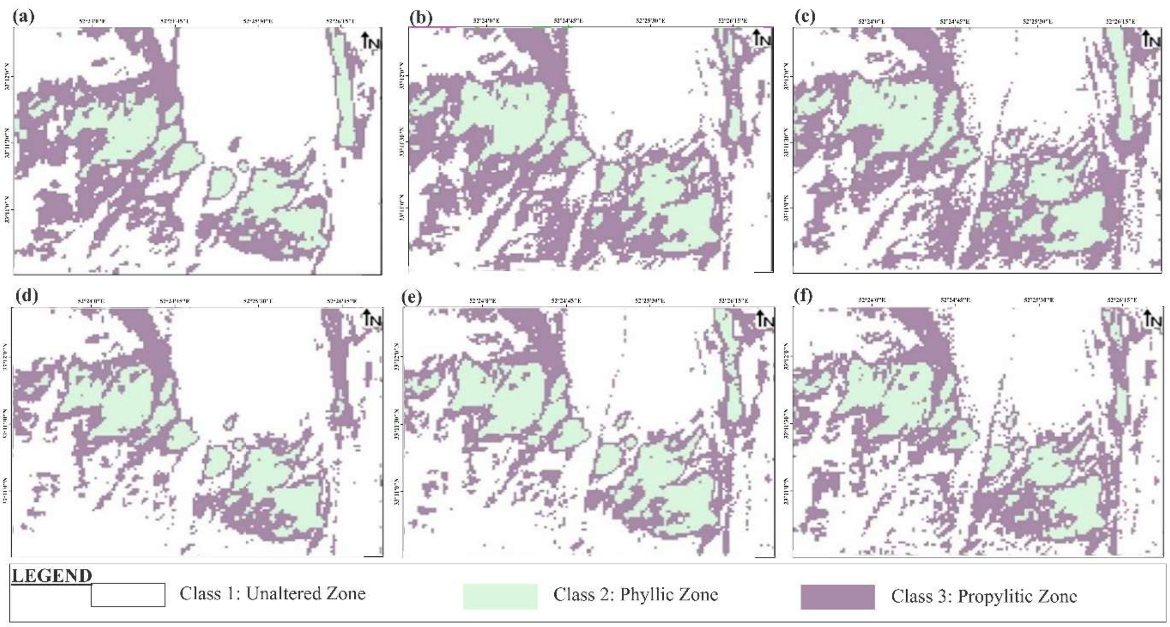

Figure 8. K-Means clustering applied to SWIR indices 4 through 9: (a) 4, (b) 5, (c) 6, (d) 7, (e) 8, (f) 9

Table 1. Accuracy of results and number of classes for K- Means clustering and SVM algorithm.

ASTER Bands	Num Classes	K-Means Cluster Evaluation/Silhouette	SVM Accuracy
Band 4	K = 3	0.76393	0.98652
Band 5		0.73228	0.97899
Band 6		0.67730	0.98914
Band 7		0.67251	0.97671
Band 8		0.73141	0.97654
Band 9		0.67242	0.98739

5.2 FCM clustering output

The FCM clustering results of different alteration categories within the study area are illustrated in Fig.9. The clustering outcomes indicate that FCM effectively identified the alteration zones, showing strong consistency with the alteration map displayed in Fig.2.

Furthermore, FCM clustering successfully detected argillic alteration in the SW and NW parts of the region, which were not explicitly highlighted in the original map. This finding suggests that, in addition to accurately distinguishing existing alteration types, the method was also capable of identifying previously unrecognized argillic alteration zones, demonstrating its potential for enhanced alteration mapping.

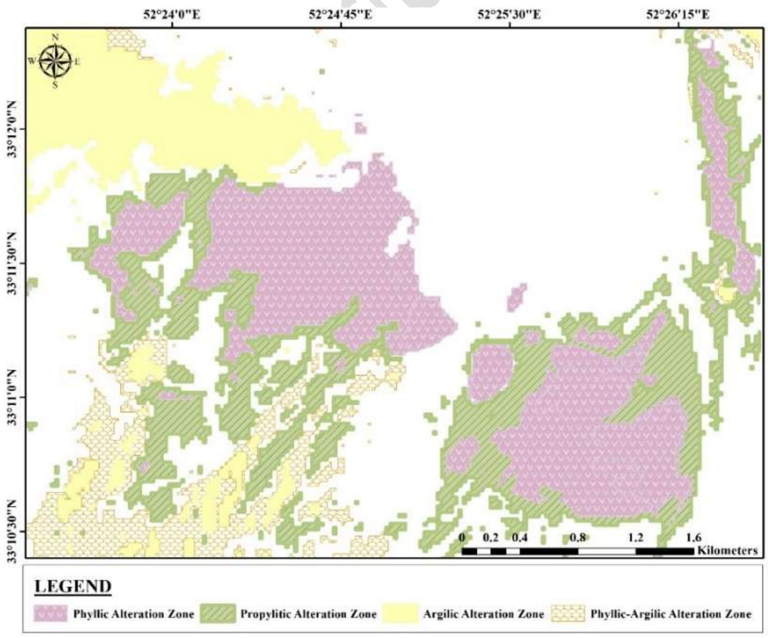

Figure 9. Resulting map and classification classes resulting from applying the FCM clustering algorithm

To evaluate the quality of the clustering performed, the Xie-Beni index was used. Xie-Beni cluster validity indices are used to evaluate the quality of FCM clustering because they could consider the geometric characteristics of the clusters. These indices evaluate the compactness and separation of clusters by measuring the intra-cluster deviations and inter-cluster distances. The results of calculating this index showed that the Xie-Beni value equals 0.25833. A low value of this index indicates appropriate cluster compactness and desirable resolution, which confirms the correct performance of the FCM algorithm.

5.3.SAM algorithm

SAM is particularly effective for distinguishing rock units by emphasizing the unique reflectance characteristics of different materials. In lithological mapping studies utilizing this approach, each rock type (lithological class) is assumed to have a distinct spectral signature (Debba et al., 2006; Rowan et al., 2006). The mean spectral signature of training samples is used as the reference spectrum, representing the spectral properties of a given class.

Propylitic alteration is characterized by absorptions from chlorite, epidote, and carbonates in ASTER bands 3 and 5 (iron and Al–OH) and in band 8 (carbonate). Argillic alteration shows bands 3, 5, and 7 absorptions linked to iron, Al–OH, and Mg–OH in kaolinite and chlorite. Similarly, phyllic alteration presents bands 3, 5, and 7 features caused by iron, Al–OH, and Mg–OH, reflecting minerals such as illite, muscovite, and chlorite (Rajendran et al., 2013; Rajendran and Nasir, 2017).

Fig.10 presents the classification maps generated using the SAM algorithm applied to the stacked image, highlighting argillic, phyllic, and propylitic alterations with their respective index minerals—kaolinite, muscovite, and chlorite.

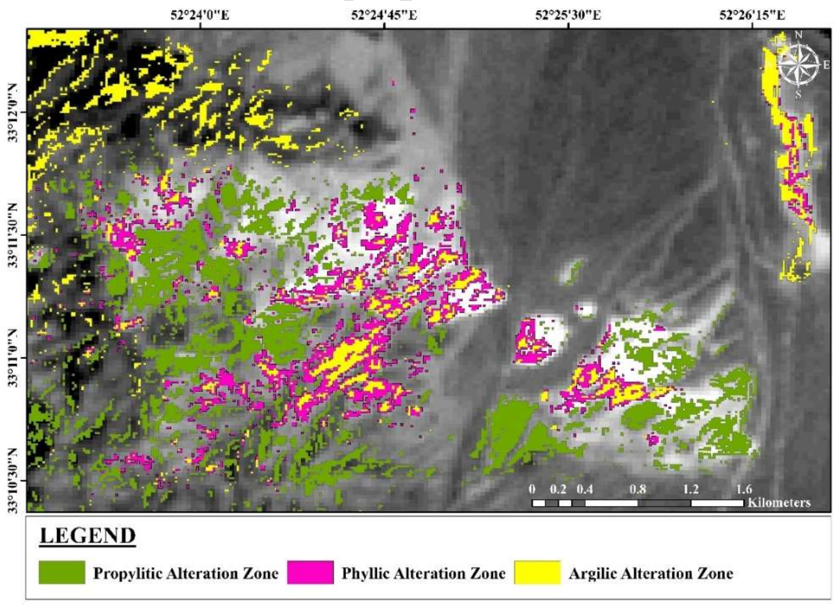

Figure 10. Hydrothermal alteration zones mapped using the SAM algorithm on ASTER satellite imagery. The map highlights three major alteration zones: Argillic alteration (yellow, associated with kaolinite), Phyllic alteration (magenta, associated with muscovite), and Propylitic alteration (green, associated with chlorite). The grayscale background represents the base satellite imagery for spatial reference

After performing FCM clustering and the SAM method, in order to examine the accuracy of alteration identification, these two outputs were overlapped with each other. Analysis of the results of combining these two methods shows that both methods have identified argillic alteration in the southwestern part of the region, which confirms the correctness of the performance of the methods used. The FCM method was able to accurately identify these areas in the southwestern and northwestern areas, where the two phyllic and argillic alterations overlap. Unlike the K-Means clustering method, which cannat identify overlapping areas, the FCM clustering method was able to separate and display these areas. In combining these two methods, it was found that the FCM clustering extracted more details from the alteration areas compared to SAM and, in some cases, identified argillic alteration in wider areas. In Fig.11 the result of the combination of two SAM and FCM clustering layers are presented, which shows how the FCM clustering was able to separate the overlapping areas of phyllic and argillic alterations correctly.

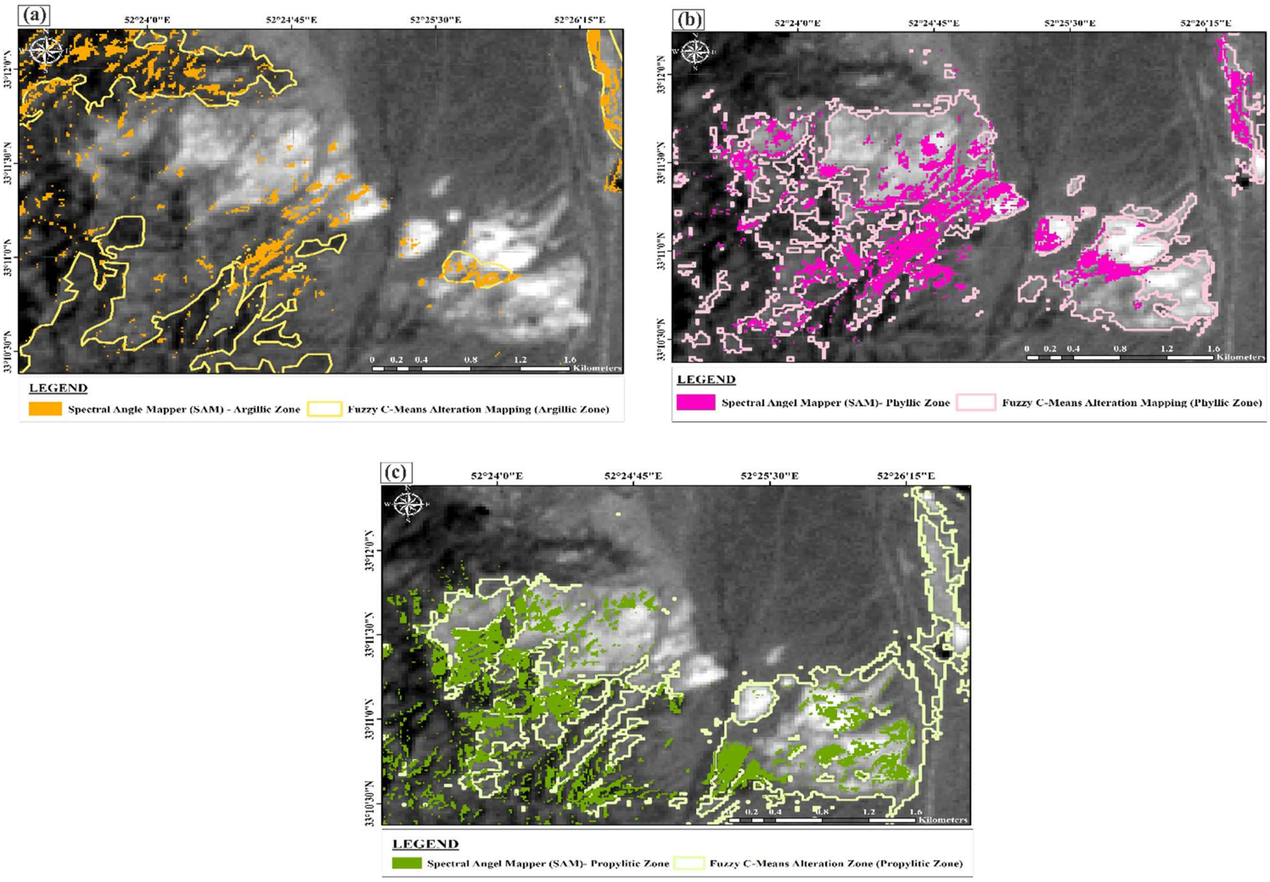

Figure 11. Comparison of hydrothermal alteration zones mapped using SAM and FCM clustering on ASTER satellite imagery. (a) Argillic alteration zone mapped by SAM (orange) and FCM clustering (yellow). (b) Phyllic alteration zone mapped by SAM (magenta) and FCM clustering (light pink). (c) Propylitic alteration zone mapped by SAM (green) and FCM clustering (light green). The grayscale background represents the base satellite imagery for spatial reference. The comparison highlights the spatial agreement and discrepancies between the two methods in identifying alteration zones

5.4.SVM model outputs

The SVM algorithm is used for classification. As a first step, the model is provided with training data and undergoes training accordingly. The result of examining the training data of this model is the classes of the K-Means clustering method. Subsequently, 70% of the samples are allocated for training and 30% for testing in the SVM model, and the model is fitted using the training set with the selected parameters and kernel. In this phase, the model is evaluated using the test data, which includes calculating the accuracy and confusion matrix, and other evaluations. Table 1 shows the accuracy of the model, and Fig.12 shows the confusion matrices of the bands on which the model is based. It was applied in individual steps. The confusion matrix illustrates the accurate distinction among the various classes. The model was able to classify most of the samples correctly. After the model evaluation, the results of applying the algorithm to different bands are presented in Fig.13. To better understand this problem, the maps in Fig. 13 were fused to the alteration map from Fig.2 (Fig.14). Finally, the bands used are stacked, which can be seen in Fig. 14, the result of the band stack.

The SVM model was able to correctly classify the image data with an accuracy of 98.25%. This performance confirmed the suitability of the RBF kernel for further classification tasks. To optimize the model, Bayesian optimization was employed to tune key hyperparameters, such as the BoxConstraint (C). The optimized values varied across spectral bands, depending on noise levels and class separability. For instance, a very high C value was observed in band 5, where the data were clean and class boundaries were well defined. In contrast, lower values were selected for noisier bands to help prevent overfitting. This adaptive behavior underscores the flexibility and effectiveness of the RBF kernel in this context. These results demonstrate the high performance of the SVM model for alteration mapping. By further optimizing the model parameters and using different kernel functions, better results can be achieved. In the following, the optimization of the model is discussed.

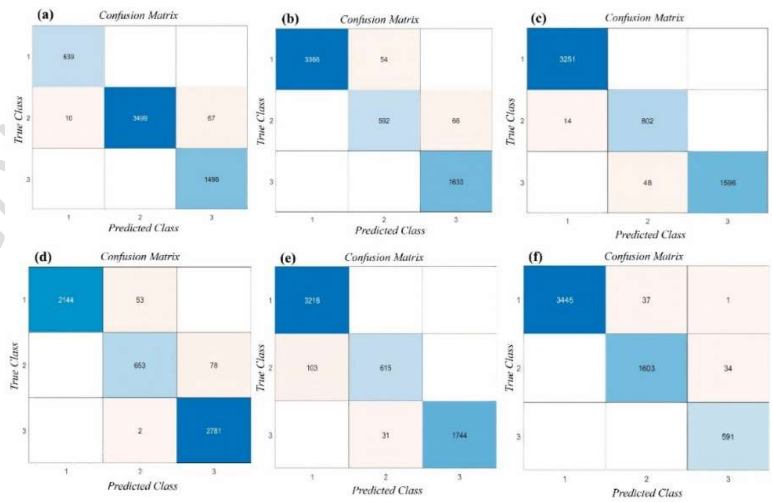

Figure 12. Band-specific confusion matrices. Bands 4-9 (a, b, c, d, e, f)

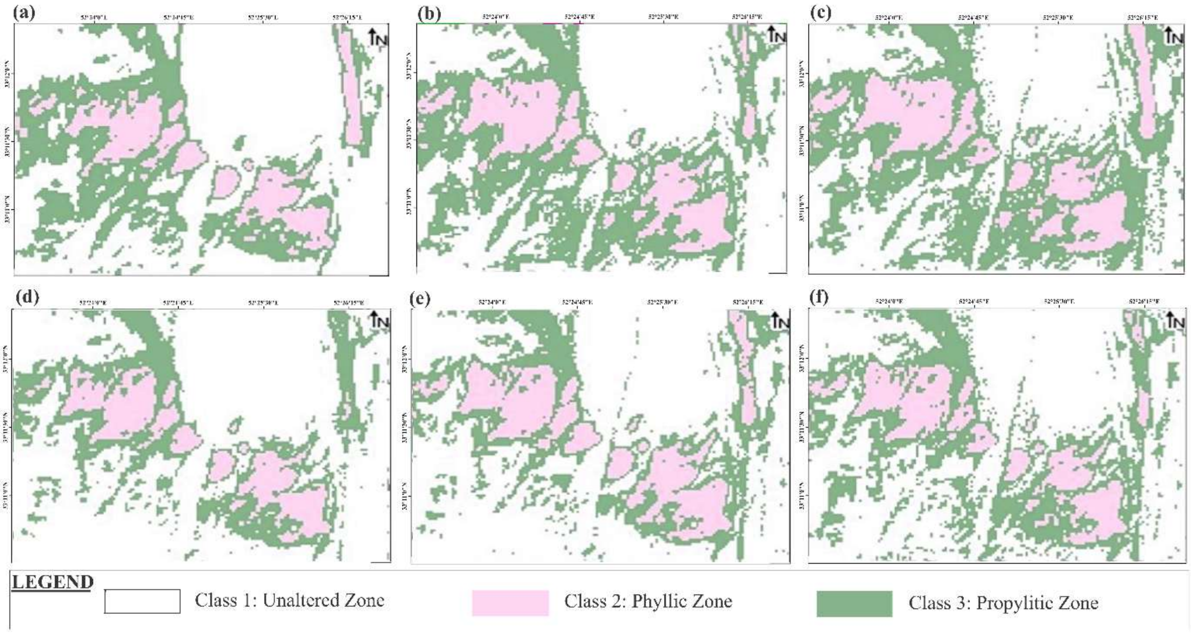

Figure 13. The results of applying the model to the SWIR bands, the green area is for propylitic alteration and the pink areas show the phyllic alteration in the studied area. Bands 4, 5, 6, 7, 8, and 9 are shown in (a), (b), (c), (d), and (f), respectively

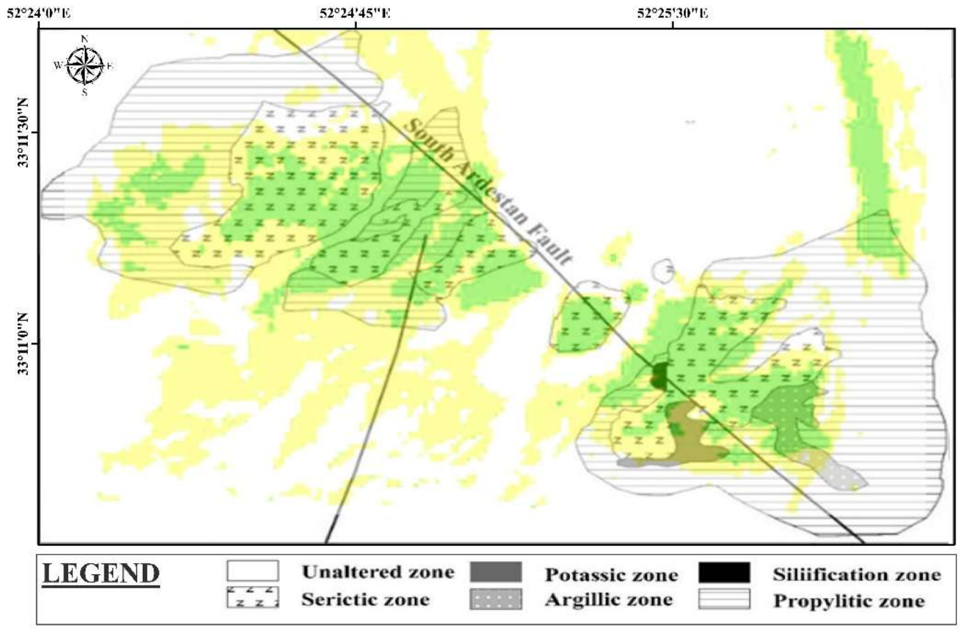

Figure 14. Displaying the overlap of SVM model results and the Zafarghand alteration map to evaluate model performance. The zones classified by the model are shown in green (phyllic) and yellow (propylitic), while the reference zones from the alteration map of the study area (Fig. 2) are illustrated using distinct patterns

5.5. Optimization SVM

In the study conducted to optimize the ML model, the Bayesian optimization method was used. This optimizer is one of the most common optimization methods in ML. The optimization in these algorithms refers to adjusting the parameters of the model to achieve adequate performance. The Bayesian method is based on statistical models that are used to search for the best operator in the hyperparameter space. The optimization results of the SVM model for the bands used are shown in Table 2. C is a parameter that helps to determine the balance between the maximum margin and the training error of the model. Table 2, which reports the optimization of the SVM model across various bands, shows that the C value for one band—specifically band 5—was greater than 990. This value was much higher than the values obtained for the other bands and requires further analysis. This band may have particular characteristics that require greater sensitivity in modeling. These features may include distinct differences between classes or unique data characteristics that warrant a high C value.

The investigations revealed that the data for this band was relatively clean and without noise. This could be seen as one of the reasons why this parameter is high, because the model was able to work more sensitively. However, in the bands where the C value is low, the data for these bands (Band 6 and Band 7) have more noise or higher scatter, so the model may need to be less sensitive to errors. This may lead to a lower C value being chosen to prevent overfitting of the model. If the classes in this band are well separated and the data is clearly delineated, the need for a high C value is reduced. A model with a lower C value can perform well without being too sensitive to errors. Consequently, C is regarded as one of the crucial hyperparameters in SVM models, exerting a notable effect on both performance and accuracy, and it must be finely tuned to obtain the best possible results (Bishop and Nasrabadi, 2006).

Table 2. Hyperparameter Settings for Classification Models.

Bands	Coding	C	KernelScale	KernelFunction	Standardize	Iteration
Band 4	Onevsone	52.082	Nan	Polynomial	True	30
Band 5	Onevsone	994.11	Nan	Linear	True	
Band 6	Onevsall	14.656	1.0192	Gaussian	True	
Band 7	Onevsall	18.302	0.0032396	Gaussian	True	
Band 8	Onevsone	460.27	Nan	Polynomial	True	
Band 9	Onevsone	852.91	0.0029307	Gaussian	True	

5.6. Comparison of model performance and accuracy on single-band vs. multi-band data

To improve the performance of the classification model, SWIR bands of the ASTER sensor were first corrected. In this process, the values of each band were normalized based on the average brightness intensity (IARR correction). This correction reduced the effect of the difference in brightness of the bands. Then, DN values were extracted from the normalized data and used as input features of the model. The process of standardizing spectral features significantly increased the model's efficiency in class separation, and this step contributed greatly to enhancing the overall accuracy achieved by the model. After correction and standardization of the spectral data, different bands were stacked together to create a multispectral dataset. Next, an initial clustering step was carried out with the K-Means algorithm. This approach automatically partitioned the dataset into four distinct groups, which then served as the main basis for the final SVM classification. After initial labeling of the data with K-Means clustering (Fig.15), a multi-class SVM model with an RBF kernel was used for final classification (Fig.16).

To increase the accuracy of the model, the values of C and KernelScale were optimized with Bayesian optimization. This adaptive method resulted in the model achieving a good balance between accuracy and generalizability with the lowest possible error. In the single-band method, each class is selected based on information from only one spectral band, so the model is not able to accurately distinguish between classes. As a result, the number of classified classes is considered less (k=3). However, in the stacked method, the combination of different spectral bands has increased the model's ability to distinguish more complex spectral patterns. This increase in input features has improved the accuracy of the model and also allowed for the separation of more classes. As a result, to provide a more accurate classification, the number of classes in the stacked method was increased from 3 to 4.

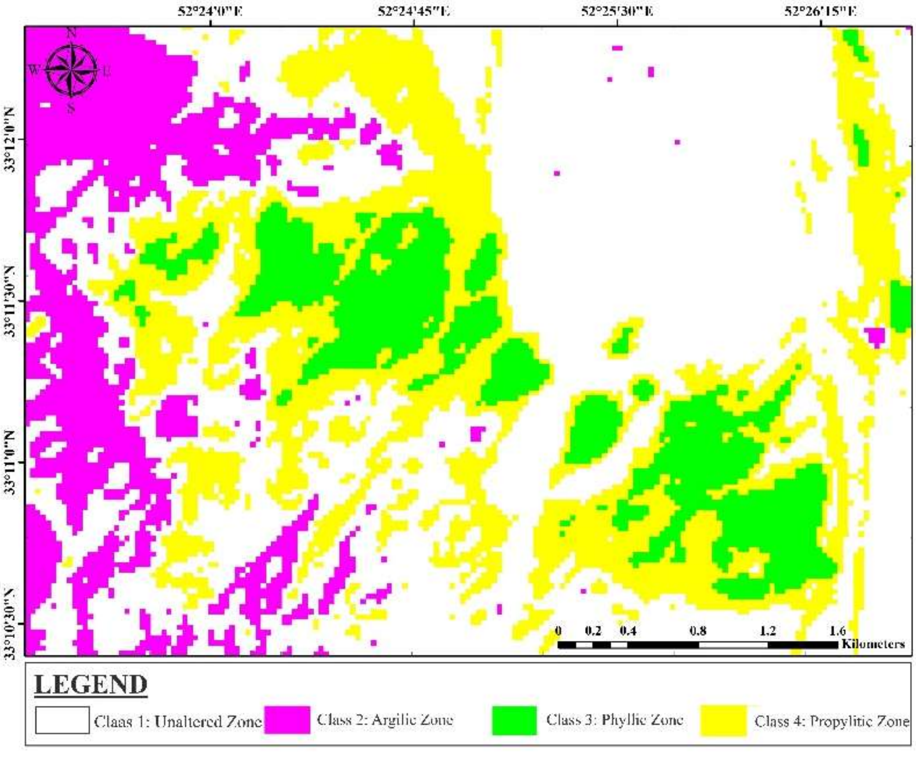

Figure 15. Hydrothermal alteration zones mapped using K-Means clustering on ASTER satellite imagery, with stacked bands 4 to 9. The classification distinguishes four major classes: (1) Unaltered zone (white), (2) Argillic alteration zone (magenta), (3) Phyllic alteration zone (green), and (4) Propylitic alteration zone (yellow). The results highlight the spatial distribution of alteration patterns, demonstrating the effectiveness of unsupervised classification in hydrothermal mapping.

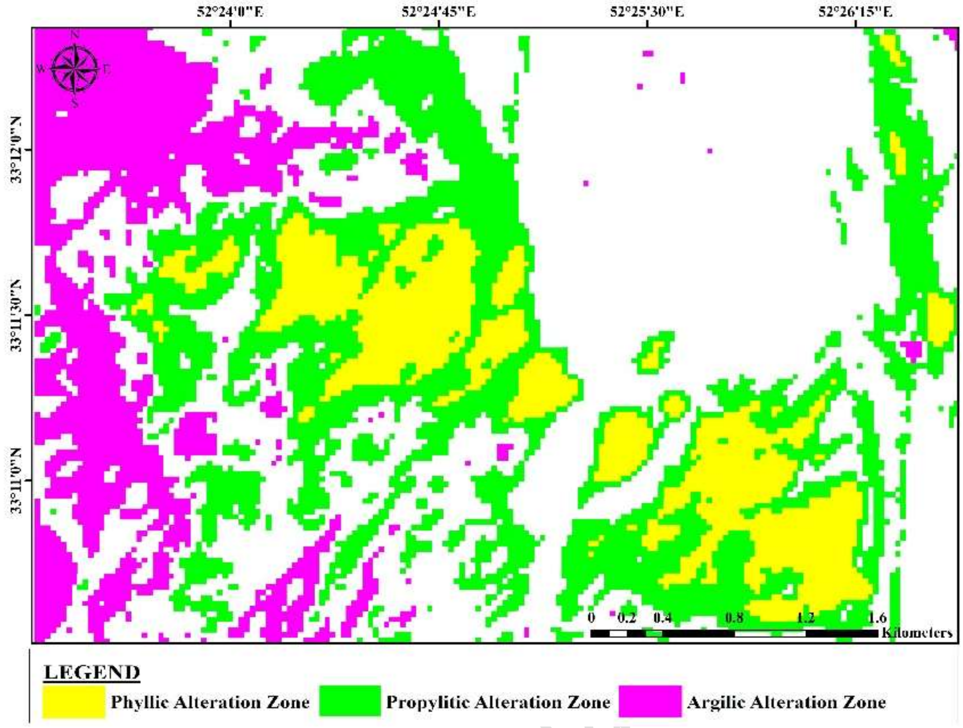

Figure 16. Hydrothermal alteration zones classified using SVM based on labeled data from K-Means clustering. The classification distinguishes three major alteration zones: Phyllic (yellow), Propylitic (green), and Argillic (magenta). The SVM model was trained using the K-Means clustering results as labeled input data, enhancing the precision of alteration zone delineation

Since the input labels of SVM are directly extracted from K-Means clustering, the SVM model tends to simulate the same patterns as K-Means clustering. Furthermore, since both K-Means clustering and SVM function on the spectral characteristics of the dataset, their resulting outputs tend to be alike. The main difference is that SVM improves the initial clusters and better separates the boundary regions by using nonlinear boundaries and an RBF kernel. To evaluate the accuracy of the model results, the classified output of SVM was compared with the regional alteration map (Fig.17). This overlap analysis showed that the model was able to accurately identify the change regions, which confirms the effectiveness of the proposed method. In the alteration map of the studied area, information about the alterations in the northeast and southwest of the area is not reported, and the map includes the northwest and southeast of the area, and the applied algorithms have been able to identify the southwest areas as argillic alteration in addition to identifying the alteration areas.

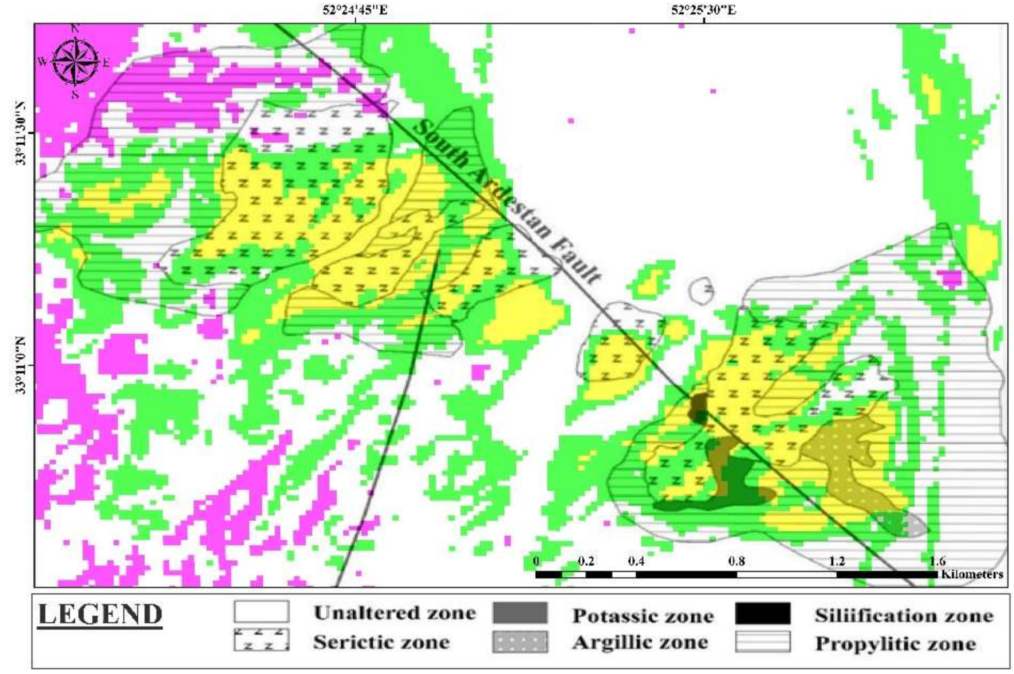

Figure 17. Validation of the hydrothermal alteration clustering results through overlapping the alteration zones identified by the ML method and the alteration map of the study area (Fig.2). The alteration zones obtained from the model are displayed in distinct colors: yellow for phyllic alteration, green for propylitic, and pink for argillic. The geological units on the map are represented with different patterns (adapted from Fig.2)

After adjusting the C and KernelScale parameters, the model reached a more realistic accuracy level of about 96%. According to the confusion matrix, the model achieves an overall accuracy value of 96.2 (Table 3). Different classes are identified with different recall rates and average precision (Precision). The F1-score value indicates the balance between Precision and Recall for each class (Table 4). The values of these indicators indicate that the model was able to separate the classes with reasonable accuracy.

Table 3. Confusion matrix of SVM classification on stacked ASTER bands

True Class/ Predicted Class	**Class 1**	**Class 2**	**Class 3**	**Class 4**
Class 1	**13200**	50	30	10
Class 2	60	**2550**	30	10
Class 3	50	20	**5500**	30
Class 4	20	15	40	**3300**

Table 4. Hyperparameters and performance metrics of the SVM model on stacked ASTER bands

BoxConstrain	KernelScale	KernelFunction	Standardize	Iteration	Accuracy	Precision	Recall	F1-score
5	3	RBF	True	100	96.2	96.5%	96.3 %	96.1 %

In the stacked method, multiple spectral bands are utilized, increasing the input information available to the model and enhancing class resolution. This enables the identification of a greater number of classes; however, it also increases model complexity and the likelihood of classification errors. As a result, while this method identifies more alteration classes, its accuracy is slightly reduced, averaging around 96%.

Findings from this investigation reveal that, in the single-band technique, the SVM model obtains accuracy around 97–98%, though it is restricted to recognizing merely three classes. The decrease in accuracy in the stacked method can be attributed to the higher complexity of the model and the increased difficulty in distinguishing between newly introduced spectral classes.

Thus, the stacked approach is beneficial for identifying a greater number of classes, even if it leads to a slight reduction in classification accuracy. In contrast, the single-band method trains the model using only a specific spectral band, which limits the number of classification classes. This reduces model complexity and enhances accuracy, as the feature space is smaller and class boundaries are more easily dened.

Table 5 presents a comparative analysis of the SVM model's performance when applied to single-band and stacked-band datasets, highlighting the trade-offs between class diversity and classification accuracy.

Table 5. Comparison of single-band and stacked-band methods for alteration mapping

Feature	Single Band method	Stacked Bands method
Num Classes	K=3	K=4
Accuracy	97-98%	96%
Inputs feature	A spectral band	Six spectral bands (SWIR4-SWIR9)
Class separation	Less, simpler	More, more complicated
Model complexity	Less	More

5.7.Field verification

Most of the rock units of the Zafarghand region have been strongly altered under the influence of hydrothermal solutions, and the resulting area of alteration covers an area of about 7 km^2, part of which is covered by sediments. Figs.18, 19 and 20 show field images, rock samples and thin sections of alteration zones in the study area. Fig.18 shows siliceous veins with copper mineralization in granodiorite rocks with intense potassic alteration, diorite rocks with strong potassic alteration, hand samples of porphyritic dacites with intense phyllic alteration, and hematite-quartz stockworks in phyllic alteration in the southern area of Zafarghand. Fig.19 shows the outcrop of phyllic and propylitic alteration, the outcrop of argillic and propylitic alteration, the microscopic image of the dacites of the argillic zone in polarized light, and the microscopic image in reflected light showing the transformation of biotite into copper sulfide in the propylitic zone. Fig.20 shows zones of secondary iron oxides in areas of copper mineralization, siliceous veins and their surrounding alteration, and quartz-magnetite veins and stockworks with malachite mineralization and iron oxide/hydroxide.

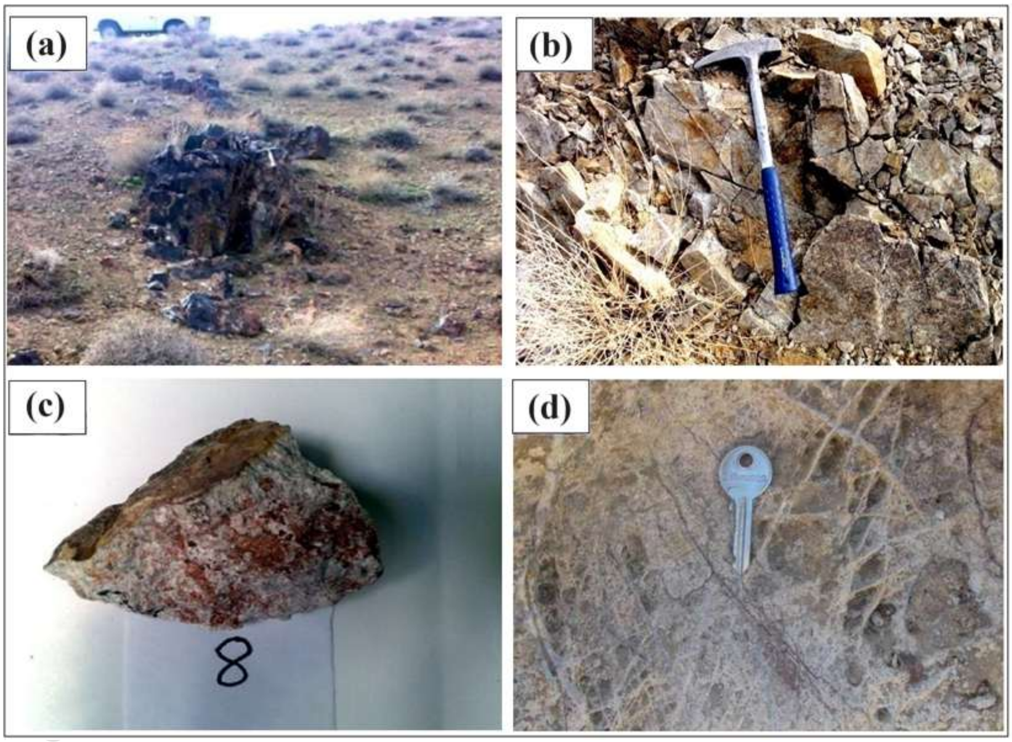

Figure 18. Field images of alterations in the study area (Ghannadpour et al., 2024). (a): Siliceous veins containing copper mineralization in granodiorite rocks with intense potassic alteration (distant view), (b): Diorite rocks with intense potassic alteration (close view), (c): Hand samples of porphyritic dacites showing intense phyllic alteration, and (d): Hematite-quartz stockworks in phyllic alteration in the southern area of Zafarghand

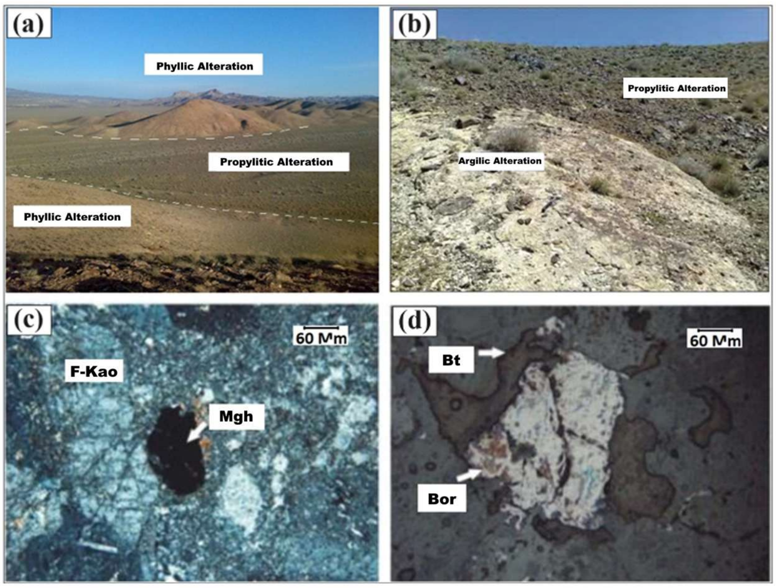

Figure 19. Microscopic and field images of rocks from the Zafarghand exploration area (Ghannadpour et al., 2024). (a): Outcrop of phyllic and propylitic alteration, (b): Outcrop of argillic and propylitic alteration, (c): Microscopic image of argillic zone dacites in polarized light, and (d): Microscopic image in reflected light corresponding to the conversion of biotite to copper sulfide in the propylitic zone. (F-Kao: Feldspar altered to kaolinite, Mgh: Magnetite, Bt: Biotite and Bor: Bornite) (Whitney and Evans, 2010)

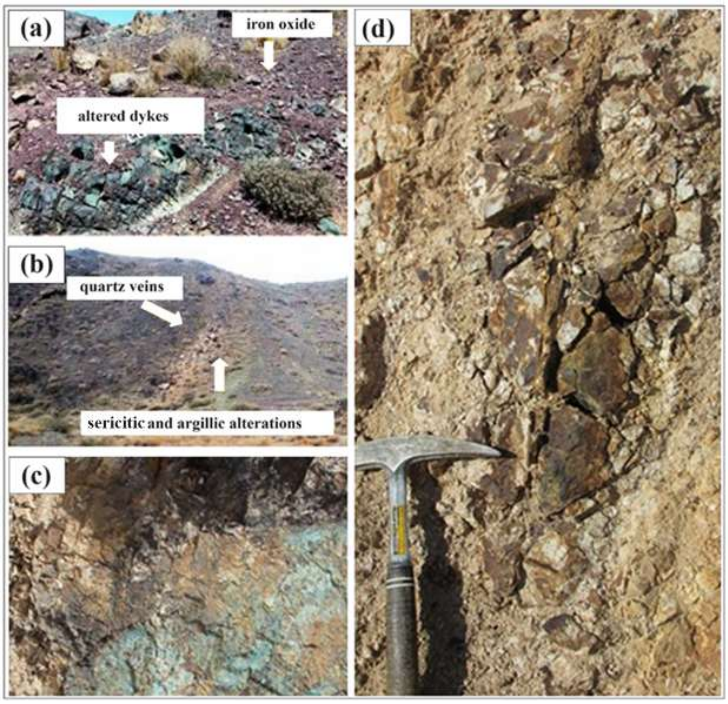

Figure 20. (a): Representation of zones with secondary iron oxides in copper mineralization areas (Esmailzadeh Kalkhoran et al 2024), (b): Siliceous veins and their surrounding alterations (Esmailzadeh Kalkhoran et al 2024), and (c) & (d): Close-up view of quartz-magnetite veins and stockworks displaying malachite mineralization and iron oxide/hydroxide (Ghannadpour et al., 2024)

In addition to field observations, petrographic studies provide clear evidence of phyllic and propylitic alteration in the Zafarghand region. In the photomicrographs shown in Fig.21, plagioclase phenocrysts—comprising approximately 25–30% of the rock volume—are extensively altered to secondary minerals such as chlorite, epidote, sericite, and kaolinite. The simultaneous presence of sericite and kaolinite indicates phyllic alteration (Fig.21a), while epidote and chlorite suggest propylitic alteration (Fig.21b). This petrographic evidence is entirely consistent with field data and the regional hydrothermal alteration model, supporting the potential presence of porphyry systems.

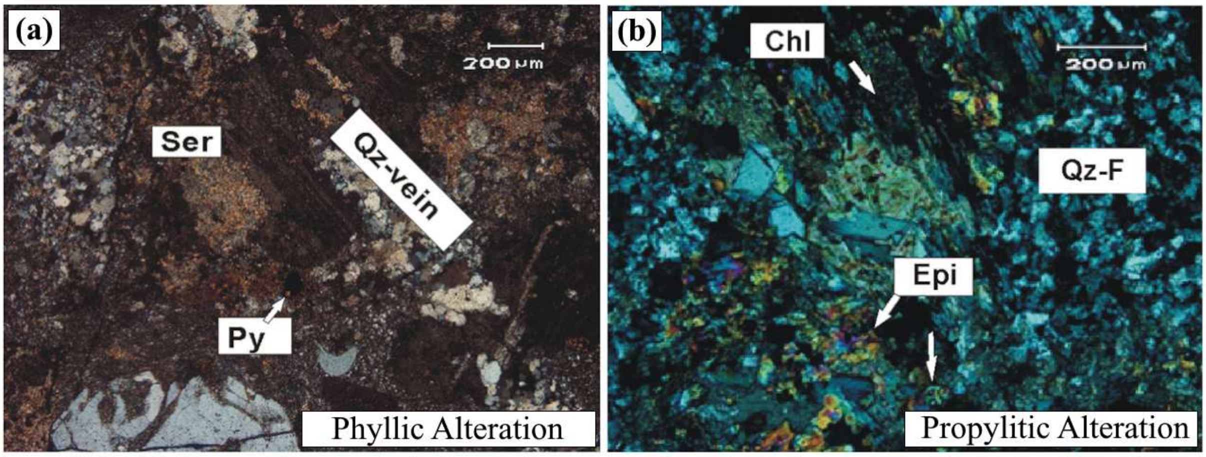

Figure 21. Petrographic images of altered samples in the Zafarghand region (a): Altered dacite porphyry texture with the presence of plagioclase phenocrysts altered to sericite and kaolinite, indicative of phyllic alteration and (b): Plagioclase altered to chlorite and epidote in an andesite matrix, indicating propylitic alteration (Aminoroayaei Yamini et al 2017)

4. Discussion

The present study employs ASTER sensor data and ML techniques for clustering and classifying alteration areas occurring across the region. ML techniques, whether supervised or unsupervised, are robust methods for managing and analyzing large datasets through classification and clustering. Combining these techniques leads to more accurate and reliable outcomes. This study aims not only to evaluate the performance of the algorithms individually and in combination, but also to identify alterations within the study area. In addition, the DNs of the satellite images and the impact of the different stages, including pre-processing and primary processing, on the overall analysis are examined. The comprehensive approach allows a detailed assessment of how the pre-processing and main processing steps affect the quality and accuracy of the results and provides a deeper understanding of their influence on alteration detection and classification.

In this work, the objective was to determine the capabilities of ML algorithms for mineral exploration purposes. In supervised algorithms, the model requires training patterns to learn and subsequently classify or cluster the original inputs. In this study, outputs from the K-Means clustering algorithm served as training data for the model, and this procedure enhanced the overall accuracy achieved by the algorithm. The study was conducted in a small study area, which allowed for a more focused analysis and higher precision of the results. As mentioned, reducing both study area extent and image resolution showed no impact on the DNs. Instead, the smaller area allowed for a higher degree of focus, suggesting that higher accuracy can be achieved compared to larger areas.

Validation of results is a crucial and fundamental aspect of satellite image processing, ensuring that the performance of the algorithm is accurately evaluated. In this study, various criteria for evaluating the models were examined, and the results were satisfactory and acceptable. This indicates that the algorithms were applied correctly and successfully identified the target of investigating porphyry Cu alteration in the region. The algorithms showed high accuracy in detecting these alterations. The alteration map of the region was used for validation, although ground data and drilling samples, which would have been ideal, were unfortunately not available for this study. Outcomes from this study show that the combination of ML approaches yields more precise results. These methods can be used effectively for the classification of satellite images. The comparison of ML methods in this study shows that while single-band SVM achieved the highest accuracy (97-98%), stacked-band SVM (96.2%) identified more alteration classes. Additionally, SAM + FCM clustering effectively detected overlapping alteration zones, enhancing mineral exploration maps. These results highlight the trade-off between accuracy and the ability to capture complex alteration patterns. An important application of these techniques is mineral exploration, assessment of mineral potential, and identification of hydrothermal alteration, such as porphyry Cu alteration. In this study, these methods were successfully applied to identify such alterations in the Zafarghand exploration area. One of the key challenges in alteration mapping is detecting areas where different alteration types overlap. This study addressed this issue by integrating FCM clustering with SAM, allowing each pixel to belong to multiple alteration types. This approach effectively highlighted overlapping alteration zones, which were less distinguishable in traditional classification methods. The ability to map such complex geological features is critical for enhancing the reliability of mineral exploration models.

Although the ASTER SWIR bands have a spatial resolution of 30 meters—which can lead to issues such as spectral noise, mixed pixels, and limited detection of small-scale features—a careful selection of a limited study area and the implementation of preprocessing steps, including radiometric calibration and IARR normalization, have significantly mitigated these challenges. These measures enhanced the spectral uniformity of the data and reduced the effects of illumination and topographic variations. To further improve the accuracy of classification and the separation of overlapping alteration zones, the SAM algorithm was combined with the FCM clustering. This soft classification approach facilitated more effective differentiation of transitional zones. Although the evaluation of results using alteration maps and field observations demonstrated satisfactory accuracy, future studies could benefit from the use of higher-resolution hyperspectral data or the integration of geophysical information such as LiDAR and magnetometry. These additions could enhance the detection of alteration features and improve the assessment of mineral potential.

5. Conclusions

The study employed ML on ASTER SWIR bands to delineate alteration zones of porphyry Cu deposits. The DNs from the selected bands were analyzed through K-Means clustering. Using this technique, similar pixels were grouped based on their spectral characteristics, and the quality of the clustering was assessed using the silhouette index. This index is a measure of how well each pixel was clustered and indicates the effectiveness of the clustering process. In the subsequent phase, the SVM model was used for classification tasks. The model was trained with a dataset, and the hyperparameters were optimized to improve the prediction accuracy. After training, the SVM model was used to predict labels for test data, and the accuracy of these predictions was evaluated. The model's performance was described through the use of confusion matrices. It was found that the SVM achieved an accuracy of 98.652% for the SWIR4 band, 97.899% for the SWIR5 band, and a high overall accuracy of 98.25% for the other bands. The K-Means clustering method was less accurate, but achieved an accuracy of 78.83%. In this study, K-Means clustering was employed as a preprocessing method to generate initial labels, which were then used as training data for the SVM model to perform the final classification. This approach improved the generalization capability of the model while reducing the need for manual data labeling. While K-Means method is an unsupervised clustering method that groups data based on spectral similarity, the SVM model operates as a supervised classifier that can define nonlinear boundaries using kernel functions. The use of K-Means clustering labels for training SVM resulted in SVM producing outputs similar to K-Means clustering, but with the added advantage of better class separation, particularly in overlapping areas. The findings of this research indicate that both K-Means clustering and SVM algorithms deliver satisfactory results. In particular, the SVM model showed exceptional accuracy in predicting the labels after optimizing the hyperparameters.

To identify areas where alteration zones overlapped, a combination of SAM and FCM clustering was applied. Unlike K-Means, the FCM clustering allows each pixel to belong to multiple classes simultaneously, making it highly effective in highlighting alteration zones with spectral overlap. The integration of these two methods demonstrated high accuracy in delineating alteration zones when compared to the regional alteration map, confirming its effectiveness in enhancing the detection of complex alteration patterns. Additionally, the SVM model applied to the stacked dataset achieved an accuracy of 96.2%, which, although slightly lower than single-band accuracy, allowed for the identification of more alteration classes, making it a valuable approach for comprehensive mineral mapping.

Furthermore, the study highlights the importance of selecting appropriate pre-processing techniques and optimizing ML models to achieve high accuracy. The success of the SVM model suggests that similar methods could be applied to multispectral and hyperspectral remote sensing data to achieve more accurate and insightful analysis. Future research could benefit from integrating additional data sources or exploring advanced ML techniques to further improve the capabilities of remote sensing image processing for mineral exploration.

Funding: This research did not receive any specific grant from funding agencies in the public, commercial, or not-for-profit sectors.

Author contributions

Seyyed Saeed Ghannadpour: Supervision of the study, analysis of results, and providing guidance throughout the research process.

Samane Esmaelzade Kalkhoran: Conducted coding, data analysis, and implementation of the manuscript.

Amin Beiranvand Pour: Provided guidance, improved the manuscript, and contributed to the overall enhancement of the manuscript.

Acknowledgments: Department of Mining Engineering, Amirkabir University of Technology (Tehran Polytechnic) is highly appreciated. The Institute of Oceanography and Environment (INOS), Univer-sity Malaysia Terengganu (UMT) is also acknowledged for providing facilities for editing, re-writing, and re-organizing the manuscript.

References

Abdullah D.M., Abdulazeez A.M. (2021) Machine learning applications based on SVM classification: *A review, Qubahan Academic Journal* 1(2): 81–90. DOI: https://doi.org/10.48161/qaj.v1n2a50

Abdalameer A.K., Alswaitti M., Alsudani A.A., Isa N.A.M. (2022) A new validity clustering index based on finding new centroid positions using the mean of clustered data to determine the optimum number of clusters, *Expert Systems with Applications* 191: 116329. DOI: https://doi.org/10.1016/j.eswa.2021.116329

Arai K., Barakbah A.R. (2007) Hierarchical K-means: An algorithm for centroid initialization in K-means, *Reports of the Faculty of Science and Engineering* 36(1): 25–31.

Aminoroayaei Yamini M., Tutti F., Haschke M., Ahmadian J., Murata M. (2017) Synorogenic copper mineralization during the Alpine–Himalayan orogeny in the Zafarghand copper exploration district, Central Iran: Petrography, geochemistry, and alteration thermometry, *Geological Journal* 52(2): 263–281. DOI: https://doi.org/10.1002/gj.2755.

Aminoroayaei Yamini M., Tutti F., Ahmadian J. (2016) Hydrothermal alteration of porphyry copper deposit in the southwest of Zafarghand with emphasis on mineralogical and geochemical changes in the area, *Journal of Earth Sciences Research* 7(25): 75–90. DOI: https://dorl.net/dor/20.1001.1.20088299.1395.7.1.6.7

Alaminia Z., Bagheri H., Salehi M. (2017) Geochemical and geophysical investigations and fluid inclusion studies in the exploration area of Zafarghand (northeast Isfahan, Iran), *Journal of Economic Geology* 9(2): 295–312. DOI: https://doi.org/10.22067/econg.v9i2.56334

Asokan A., Anitha J., Ciobanu M., Gabor A., Naaji A., Hemanth D.J. (2020) Image processing techniques for analysis of satellite images for historical maps classification: An overview, *Applied Sciences* 10(12): 4207. DOI: https://doi.org/10.3390/app10124207

Babbar J., Rathee N. (2019) Satellite image analysis: A review, Proceedings of the 2019 IEEE International Conference on Electrical, Computer and Communication Technologies (ICECCT): 1–6.

Benediktsson J.A., Palmason J.A., Sveinsson J.R. (2005) Classification of hyperspectral data from urban areas based on extended morphological profiles, *IEEE Transactions on Geoscience and Remote Sensing* 43(3): 480–491.

Bekaddour A., Bessaid A., Bendimerad F.T. (2015) Multispectral satellite image ensemble classification combining K-means, LVQ, and SVM classification techniques, *Journal of the Indian Society of Remote Sensing* 43: 671–686. DOI: https://doi.org/10.1007/s12524-014-0445-x

Bezdek J.C. (2013) Pattern recognition with fuzzy objective function algorithms, *Springer Science & Business Media*.

Bishop C.M., Nasrabadi N.M. (2006) Pattern recognition and machine learning. New York: springer 17.

Bishop J.L., Murad E. (2005) The visible and infrared spectral properties of jarosite and alunite, *American Mineralogist* 90: 1100–1107. DOI: https://doi.org/10.2138/am.2005.1700

Camps-Valls G., Bruzzone L. (2005) Kernel-based methods for hyperspectral image classification, *IEEE Transactions on Geoscience and Remote Sensing* 43(6): 1351–1362. DOI: https://doi.org/10.1109/TGRS.2005.846154

Carranza E.J., Laborte A.G. (2016) Data-driven predictive modeling of mineral prospectivity using random forests: A case study in Catanduanes Island (Philippines), *Natural Resources Research* 25: 35–50. DOI: https://doi.org/10.1007/s11053-015-9268-x

Clark R.N., King T.V., Klejwa M., Swayze G.A., Vergo N. (1990) High spectral resolution reflectance spectroscopy of minerals, *Journal of Geophysical Research: Solid Earth* 95(B8): 12653–12680.

Clark R.N., Swayze G.A., Gallagher A.J., King T.V., Calvin W.M. (1993) The US Geological Survey digital spectral library: Version 1 (0.2 to 3.0 μm) (No. 93-592), *U.S. Geological Survey*.

Cortes C. (1995) Support-vector networks, *Machine Learning* 20: 273–297. DOI: https://doi.org/10.1007/BF00994018

Chen X., Warner T.A., Campagna D.J. (2007) Integrating visible, near-infrared, and short-wave infrared hyperspectral and multispectral thermal imagery for geological mapping at Cuprite, Nevada, *Remote Sensing of Environment* 110(3): 344–356. DOI: https://doi.org/10.1016/j.rse.2007.02.006

Dalton J.B., Bove D.J., Mladinich C.S., Rockwell B.W. (2004) Identification of spectrally similar materials using the USGS Tetracorder algorithm: The calcite–epidote–chlorite problem, *Remote Sensing of Environment* 89(4): 455–466.

Debba P., Carranza E.J., van der Meer F.D., Stein A. (2006) Abundance estimation of spectrally similar minerals using derivative spectra in simulated annealing, *IEEE Transactions on Geoscience and Remote Sensing* 44(12): 3649–3658.

Del Frate F., Pacifici F., Schiavon G., Solimini C. (2007) Use of neural networks for automatic classification from high-resolution images, *IEEE Transactions on Geoscience and Remote Sensing* 45(4): 800–809. DOI: https://doi.org/10.1109/TGRS.2007.892009

El-Qassas R.A., Abu-Donia A.M., Omar A.E. (2023) Delineation of hydrothermal alteration zones associated with mineral deposits using remote sensing and airborne geophysics data: A case study from the El-Bakriya area, Central Eastern Desert, Egypt, *Acta Geodaetica et Geophysica* 58(1): 71–107. DOI: https://doi.org/10.1007/s40328-023-00405-y

Esmailzadeh Kalkhoran S., Ghannadpour S.S., Jalili H., Moeini Rad A. (2024) Investigating porphyry copper alterations and spectral behavior of related minerals using ASTER satellite images in the Zafarghand region, Isfahan, *Advanced Applied Geology*, in press. DOI: https://doi.org/10.22055/aag.2024.45697.2425

Esmaelzadeh Kalkhoran S., Ghannadpour S.S., Moeini Rad A., Jalili H. (2024) Comparing the performance of ASTER and Landsat-8 satellite images in identifying iron oxide and porphyry copper alterations in the Zafarghand region of Isfahan Province, *Journal of Mineral Resources Engineering* 9(1): 41–65. DOI: https://doi.org/10.30479/jmre.2023.19459.1669

Fallaha M., Jamali H., Alaminia Z., Pour A.B. (2024) ASTER remote sensing data for detecting porphyry copper-type alteration patterns in the West Zafarghand Cu±Mo deposit, Iran, *International Journal of Image and Data Fusion*, in press. DOI: https://doi.org/10.1080/19479832.2024.2429589

Foody G.M., Mathur A. (2004) Toward intelligent training of supervised image classifications: Directing training data acquisition for SVM classification, *Remote Sensing of Environment* 93(1–2): 107–117. DOI: https://doi.org/10.1016/j.rse.2004.06.017

Fu Y., Cheng Q., Jing L., Ye B., Fu H. (2023) Mineral prospectivity mapping of porphyry copper deposits based on remote sensing imagery and geochemical data in the Duolong ore district, Tibet, *Remote Sensing* 15(2): 439. DOI: https://doi.org/10.3390/rs15020439

Gewali U.B., Monteiro S.T., Saber E. (2018) Machine learning-based hyperspectral image analysis: A survey, *arXiv preprint* arXiv:1802.08701. DOI: https://doi.org/10.48550/arXiv.1802.08701

Ghannadpour S.S., Hezarkhani A. (2023) Relationship between rare earth and radioactive elements, *Iranian Journal of Earth Sciences* 15(2): 142–154. DOI: https://doi.org/10.30495/ijes.2022.1942984.1698

Ghannadpour S.S., Esmaelzadeh Kalkhoran S. (2024a) Using the singularity method in identifying the alterations in the Zafarghand porphyry copper deposit (Isfahan), *Advanced Applied Geology* 14(2): 45–60. DOI: https://doi.org/10.22055/aag.2024.46480.2446

Ghannadpour S.S., Esmaelzadeh Kalkhoran S., Behifar M., Jalili H. (2024) Delineation of the alteration zones by CN fractal model on ASTER images, *Journal of Mining and Environment* 15(3): 1001–1016. DOI: https://doi.org/10.22044/jme.2024.14644.2765

Ghannadpour S.S., Hasiri M., Jalili H., Talebiesfandarani S. (2024b) Satellite image processing: Application for alteration separation based on U-statistic method in Zafarghand porphyry system (Iran), *Journal of Mining and Environment* 15(2): 667–681. DOI: https://doi.org/10.22044/jme.2023.13652.2525

Grove C.I., Hook S.J., Paylor E.D. III (1992) Laboratory reflectance spectra of 160 minerals, 0.4 to 2.5 µm, *Jet Propulsion Laboratory Publication* 92-2, Pasadena, California, 134 p.

Gupta R. (2003) Remote Sensing Geology, 2nd ed. *Springer*, Berlin, 655 p. DOI: https://doi.org/10.1007/978-3-662-05283-9

Hecker C., van der Meijde M., van der Werff H., van der Meer F.D. (2008) Assessing the influence of reference spectra on synthetic SAM classification results, *IEEE Transactions on Geoscience and Remote Sensing* 46(12): 4162–4172.

Huang C., Davis L.S., Townshend J.R. (2002) An assessment of support vector machines for land cover classification, *International Journal of Remote Sensing* 23(4): 725–749. DOI: https://doi.org/10.1080/01431160110040323

Hunt G.R. (1971) Visible and near-infrared spectra of minerals and rocks: II. Carbonates*, Modern Geology* 2: 23–30.

Jain R., Bhu H., Pandey A.K., Pour A.B. (2025) Base-metal exploration using remote sensing, geological, geophysical, and geochemical datasets with clues from ancient mining: A comprehensive review on Aravalli–Delhi Fold Belt, Rajasthan, India, *Advances in Space Research* 75(1): 277–315. DOI: https://doi.org/10.1016/j.asr.2024.09.038

Kavzoglu T., Colkesen I. (2009) A kernel functions analysis for support vector machines for land cover classification, *International Journal of Applied Earth Observation and Geoinformation* 11(5): 352–359. DOI: https://doi.org/10.1016/j.jag.2009.06.002

Khaleghi M., Ranjbar H., Abedini A., Calagari A.A. (2020) Synergetic use of the Sentinel-2, ASTER, and Landsat-8 data for hydrothermal alteration and iron oxide minerals mapping in a mine scale, *Acta Geodynamica et Geomaterialia* 17(3): 285–296. DOI: https://doi.org/10.13168/AGG.2020.0023

Khosaravi M., Saadat S, Dabiri R. (2020) Evaluation of heavy metal contamination in soil and water resources around Taknar copper mine (NE Iran), *Iranian Journal of Earth Sciences* 12 (3), 212-222. DOI: https://doi.org/10.30495/ijes.2020.675578

Kruse F.A., Lefkoff A.B., Boardman J.W., Heidebrecht K.B., Shapiro A.T., Barloon P.J., Goetz A.F. (1993) The spectral image processing system (SIPS)—interactive visualization and analysis of imaging spectrometer data, *Remote Sensing of Environment* 44(2–3): 145–163.

Kumar C., Shetty A., Raval S., Sharma R., Ray P.C. (2015) Lithological discrimination and mapping using ASTER SWIR data in the Udaipur area of Rajasthan, India, *Procedia Earth and Planetary Science* 11: 180–188. DOI: https://doi.org/10.1016/j.proeps.2015.06.022

Li Y., Shen Y. (2010) Fuzzy C-means clustering based on spatial neighborhood information for image segmentation, *Journal of Systems Engineering and Electronics* 21(2): 323–328.

Li Q., Zhang B., Lu L., Lin Q. (2014) Hydrothermal alteration mapping using ASTER data in Baogutu porphyry deposit, China, *IOP Conference Series: Earth and Environmental Science* 17(1): 012174. IOP Publishing. DOI: https://doi.org/10.1088/1755-1315/17/1/012174

Lowell J.D., Guilbert J.M. (1970) Lateral and vertical alteration–mineralization zoning in porphyry ore deposits, *Economic Geology* 65(4): 373–408. DOI: https://doi.org/10.2113/gsecongeo.65.4.373

Lu J., Han L., Liu L., Wang J., Xia Z., Jin D., Zha X. (2023) Lithology classification in semi-arid areas combining multi-source remote sensing images using support vector machine optimized by improved particle swarm algorithm, *International Journal of Applied Earth Observation and Geoinformation* 119: 103318. DOI: https://doi.org/10.1016/j.jag.2023.103318

Mahesh B. (2020) Machine learning algorithms: A review, *International Journal of Science and Research* (IJSR) 9(1): 381–386. DOI: https://doi.org/10.21275/ART20203995

Mars J.C., Rowan L.C. (2006) Regional mapping of phyllic- and argillic-altered rocks in the Zagros magmatic arc, Iran, using Advanced Spaceborne Thermal Emission and Reflection Radiometer (ASTER) data and logical operator algorithms, *Geosphere* 2(3): 161–186. DOI: https://doi.org/10.1130/GES00044.1

Maxwell A.E., Warner T.A., Fang F. (2018) Implementation of machine-learning classification in remote sensing: An applied review, *International Journal of Remote Sensing* 39(9): 2784–2817. DOI: https://doi.org/10.1080/01431161.2018.1433343

Maulik U., Bandyopadhyay S. (2000) Genetic algorithm-based clustering technique, *Pattern Recognition* 33(9): 1455–1465. DOI: https://doi.org/10.1016/S0031-3203(99)00137-5

Mitchell T.M. (1997) Does machine learning really work? *AI Magazine* 18(3): 11–20. DOI: https://doi.org/10.1609/aimag.v18i3.1303

Mhangara P. (2005) Testing the ability of ASTER (Advanced Spaceborne Thermal Emission and Reflection Radiometer) to map hydrothermal alteration zones: A case study of the Haib porphyry copper–molybdenum deposit, Namibia, *Doctoral dissertation, Stellenbosch University, Stellenbosch*. DOI: http://hdl.handle.net/10019.1/50462

Moghadam A. R., Lotfi M., Jafari M. R., Ashja Ardalan A., Pour Moghaddam M., Yazdi A. (2021) Economic Geology, Petrology and Environmental of Copper Ore Deposits of Chagho in South West Karaj, *Revista Geoaraguaia,* 11(1), 7-26.

Mohammadi S., Nadimi A., Alaminia Z. (2018) Analysis of the relationship between mineralization and alteration zones with tectonic structures using remote sensing studies in the south Ardestan area (northeastern Isfahan), *Journal of Tectonics* 2(7): 29–49. DOI: https://doi.org/10.22077/JT.2020.2434.1013

Mountrakis G., Im J., Ogole C. (2011) Support vector machines in remote sensing: A review, *ISPRS Journal of Photogrammetry and Remote Sensing* 66(3): 247–259. DOI: https://doi.org/10.1016/j.isprsjprs.2010.11.001

Moradpour H., Rostami Paydar G., Feizizadeh B., Blaschke T., Pour A.B., Valizadeh Kamran K., Muslim A.M., Hossain M.S. (2022) Fusion of ASTER satellite imagery, geochemical and geological data for gold prospecting in the Astaneh granite intrusive, West Central Iran, *International Journal of Image and Data Fusion* 13(1): 71–94. DOI: https://doi.org/10.1080/19479832.2021.1915395

Murphy R.J., Monteiro S.T., Schneider S. (2012) Evaluating classification techniques for mapping vertical geology using field-based hyperspectral sensors, *IEEE Transactions on Geoscience and Remote Sensing* 50(8): 3066–3080.

Osisanwo F.Y., Akinsola J.E., Awodele O., Hinmikaiye J.O., Olakanmi O., Akinjobi J. (2017) Supervised machine learning algorithms: Classification and comparison, *International Journal of Computer Trends and Technology (IJCTT)* 48(3): 128–138. DOI: https://doi.org/10.14445/22312803/IJCTT-V48P126

Naeem S., Ali A., Anam S., Ahmed M.M. (2023) An unsupervised machine learning algorithm: A comprehensive review, *International Journal of Computing and Digital Systems* 13(1): 172–190. DOI: https://doi.org/10.12785/ijcds/130172

Pal M. (2005) Random forest classifier for remote sensing classification, *International Journal of Remote Sensing* 26(1): 217–222. DOI: https://doi.org/10.1080/01431160412331269698

Pal M., Foody G.M. (2012) Evaluation of SVM, RVM, and SMLR for accurate image classification with limited ground data, *IEEE Journal of Selected Topics in Applied Earth Observations and Remote Sensing* 5(5): 1344–1355. DOI: https://doi.org/10.1109/JSTARS.2012.2215310

Pour A.B., Hashim M. (2012) The application of ASTER remote sensing data to porphyry copper and epithermal gold deposits, *Ore Geology Reviews* 44: 1–9. DOI: https://doi.org/10.1016/j.oregeorev.2011.09.009

Pour A.B., Hashim M. (2011) Identification of hydrothermal alteration minerals for exploration of porphyry copper deposit using ASTER data, SE Iran, Journal of Asian Earth Sciences 42(6): 1309–1323. https://doi.org/10.1016/j.jseaes.2011.07.017.

Rahmani N., Sekandari M., Pour A.B., Ranjbar H., Nezamabadi Pour H., Carranza E.J.M. (2025) Evaluation of support vector machine classifiers for lithological mapping using PRISMA hyperspectral remote sensing data: Sahand–Bazman magmatic arc, Central Iran, *Remote Sensing*

Applications: Society and Environment 37: 101449. DOI: https://doi.org/10.1016/j.rsase.2025.101449

Rajendran S., Nasir S., Kusky T.M., Ghulam A., Gabr S., El-Ghali M.A. (2013) Detection of hydrothermal mineralized zones associated with listwaenites in Central Oman using ASTER data, *Ore Geology Reviews* 53: 470–488. DOI: https://doi.org/10.1016/j.oregeorev.2013.02.008

Rajendran S., Nasir S. (2017) Characterization of ASTER spectral bands for mapping of alteration zones of volcanogenic massive sulphide deposits, *Ore Geology Reviews* 88: 317–335. DOI: https://doi.org/10.1016/j.oregeorev.2017.04.016

Ramsey M.S., Flynn I.T. (2020) The spatial and spectral resolution of ASTER infrared image data: A paradigm shift in volcanological remote sensing, *Remote Sensing* 12(4): 738. DOI: https://doi.org/10.3390/rs12040738

Rowan L.C., Schmidt R.G., Mars J.C. (2006) Distribution of hydrothermally altered rocks in the Reko Diq, Pakistan mineralized area based on spectral analysis of ASTER data, *Remote Sensing of Environment* 104(1): 74–87. DOI: https://doi.org/10.1016/j.rse.2006.05.014

Sadeghian M., Ghaffary M. (2011) The petrogenesis of Zafarghand granitoid pluton (SE of Ardestan), *Petrological Journal* 2(6): 47–70.

Sadek M.F., Ali-Bik M.W., Hassan S.M. (2015) Late Neoproterozoic basement rocks of Kadabora-Suwayqat area, Central Eastern Desert, Egypt: Geochemical and remote sensing characterization, *Arabian Journal of Geosciences* 8: 10459–10479. DOI: https://doi.org/10.1007/s12517-015-1973-6

Salisbury J.W., D'Aria D.M. (1992) Emissivity of terrestrial materials in the 8–14 μm atmospheric window, *Remote Sensing of Environment* 42(2): 83–106. DOI: https://doi.org/10.1016/0034-4257(92)90092-X

Salkuti S.R. (2020) A survey of big data and machine learning, *International Journal of Electrical and Computer Engineering* 10(1): 575–580. DOI: https://doi.org/10.11591/IJECE.V10I1.PP575-580

Sun A.Y., Scanlon B.R. (2019) How can big data and machine learning benefit environment and water management: A survey of methods, applications, and future directions, *Environmental Research Letters* 14(7): 073001. DOI: https://doi.org/10.1088/1748-9326/ab1b7d

Shuo W., Ming M. (2022) Exploring online intelligent teaching method with machine learning and SVM algorithm, *Neural Computing and Applications* 34(4): 2583–2596. DOI: https://doi.org/10.1007/s00521-021-05846-6

Shahi H., Kamkar Rouhani A. (2014) A GIS-based weights-of-evidence model for mineral potential mapping of hydrothermal gold deposits in the Torbat-e Heydarieh area, *Journal of Mining and Environment* 5(2): 79–89. DOI: https://doi.org/10.22044/jme.2014.324

Tou J.T., Gonzalez R.C. (1974). Pattern recognition principles.

Varmazyari Z., Ghannadpour S.S., Katibeh H. (2025) Determination of cobalt concentration using nonlinear regression and Monte Carlo simulation in the Zafarghand region, Isfahan, *Iranian Journal of Earth Sciences* 17(1): 1–9. DOI: https://doi.org/10.57647/j.ijes.2025.1701.08.

Vicente L.E., de Souza Filho C.R. (2011) Identification of mineral components in tropical soils using reflectance spectroscopy and Advanced Spaceborne Thermal Emission and Reflection Radiometer (ASTER) data, *Remote Sensing of Environment* 115(8): 1824–1836. DOI: https://doi.org/10.1016/j.rse.2011.02.023

Wang F., Franco-Penya H.H., Kelleher J.D., Pugh J., Ross R. (2017) An analysis of the application of simplified silhouette to the evaluation of K-means clustering validity, Machine Learning and Data Mining in Pattern Recognition: 13th International Conference, MLDM 2017, New York, USA, July 15–20, 2017, Proceedings 13: 291–305. *Springer International Publishing*. DOI: https://doi.org/10.1007/978-3-319-62416-7_21

Whitney D.L., Evans B.W. (2010) Abbreviations for names of rock-forming minerals, *American Mineralogist 95(1): 185–187*. DOI: https://doi.org/10.2138/am.2010.3371

Yousefi M., Tabatabaei S.H., Rikhtehgaran R., Pour A.B., Pradhan B. (2021) Application of Dirichlet process and support vector machine techniques for mapping alteration zones associated with porphyry copper deposit using ASTER remote sensing imagery, *Minerals* 11(11): 1235. DOI: https://doi.org/10.3390/min11111235

Yousefi T., Aliyari F., Abedini A., Calagari A.A. (2018) Integrating geologic, Landsat-8, and ASTER remote sensing data for gold exploration: A case study from Zarshuran Carlin-type gold deposit, NW Iran, *Arabian Journal of Geosciences* 11: 1–19. DOI: https://doi.org/10.1007/s12517-018-3822-x

Zuo R., Carranza E.J.M. (2023) Machine learning-based mapping for mineral exploration, *Mathematical Geosciences* 55(7): 891–895. DOI: https://doi.org/10.1007/s11004-023-10097-3